



HAL
open science

Magnetic susceptibility controlled by climate-driven weathering intensity

Jérémie Aubineau, Paul YJ Antonio, Radouan El Bamiki, Fleurice Parat, Pierre Camps, Otmane Raji, Es-Said Jourani, Jean-Louis Bodinier, Mélina Macouin, Stuart Gilder, et al.

► **To cite this version:**

Jérémie Aubineau, Paul YJ Antonio, Radouan El Bamiki, Fleurice Parat, Pierre Camps, et al.. Magnetic susceptibility controlled by climate-driven weathering intensity. Bulletin de la Société Géologique de France, In press. hal-04789430

HAL Id: hal-04789430

<https://hal.science/hal-04789430v1>

Submitted on 18 Nov 2024

HAL is a multi-disciplinary open access archive for the deposit and dissemination of scientific research documents, whether they are published or not. The documents may come from teaching and research institutions in France or abroad, or from public or private research centers.

L'archive ouverte pluridisciplinaire **HAL**, est destinée au dépôt et à la diffusion de documents scientifiques de niveau recherche, publiés ou non, émanant des établissements d'enseignement et de recherche français ou étrangers, des laboratoires publics ou privés.

1 **Magnetic susceptibility controlled by climate-driven weathering intensity**

2
3 **La susceptibilité magnétique contrôlée par l'intensité de l'altération climatique**

4
5 Jérémy Aubineau^{1,2,6*}, Paul Y. J. Antonio^{2,3,6}, Radouan El Bamiki⁴, Fleurice Parat²,
6 Pierre Camps², Otmane Raji⁴, Es-Said Jourani⁴, Jean-Louis Bodinier⁴, Mélina
7 Macouin¹, Stuart Gilder⁵, Sonia Rousse¹ & Michel Séranne²

8
9 ¹Géosciences Environnement Toulouse, CNRS UMR 5563 (CNRS/UPS/IRD/CNES), Université de
10 Toulouse, Observatoire Midi-Pyrénées, Toulouse, France

11 ²Géosciences Montpellier, Université de Montpellier, CNRS UMR 5243, Montpellier, France

12 ³Centre for Planetary Habitability (PHAB), University of Oslo, Oslo, Norway

13 ⁴Geology and Sustainable Mining Institute, Mohammed VI Polytechnic University, Ben Guerir, 43150,
14 Morocco

15 ⁵Department of Earth and Environmental Sciences, Ludwig Maximilians University, Munich, Germany

16 ⁶These authors contributed equally: J. Aubineau and PYJ. Antonio.

17
18 *Corresponding author: jeremie.aubineau@get.omp.eu

20 **Abstract**

21 Magnetic susceptibility (MS) variations are commonly attributed to eustatic and/or
22 climatic changes that impact the delivery of fine-grained detrital magnetic minerals.
23 However, the mechanism responsible for sourcing magnetic minerals from land to
24 the ocean is not fully understood. Bulk mineralogy, Rietveld refinements of powder
25 XRD patterns, and whole-rock geochemistry, combined with a MS investigation
26 across a ~290 m-thick Upper Cretaceous/Paleogene sedimentary sequence at
27 Ergueta, Morocco, imply that iron is exclusively detrital in origin. Moreover, MS
28 fluctuations occurred independently from depositional setting and sea-level
29 variations. Rock magnetism investigations further show that a complex assemblage
30 of ferromagnetic *sensu lato* minerals is recorded in the Ergueta sedimentary section,
31 and a proportion of more or less oxidized magnetite supplied to the depositional
32 setting controls the MS variations. This study chronicles that the weathering of the
33 Anti-Atlas crystalline basement led to the supply of detrital Fe-bearing phyllosilicates
34 and ferromagnetic (*sensu lato*) Fe-oxides to the eastern passive margin of the
35 Atlantic Ocean from the Late Cretaceous to the mid-Paleogene. Higher weathering
36 intensity drove up the detrital magnetic material in all lithologies, which, in turn,
37 increased the MS signal. Importantly, this model nicely coincides with the climatic
38 upheavals of the Paleogene. We propose that this unrecognized link between MS
39 and climate-driven weathering intensity is paramount to unraveling the origin of the
40 low MS interval below the Cretaceous-Paleogene boundary. Climate cooling resulting
41 in reduced weathering rather than a global acidification triggered by Phase 2 of
42 Deccan volcanism could help explain the MS trend at that time.

43

44 Keywords: Magnetic susceptibility, weathering, climate, Cretaceous/Paleogene,
45 Ergueta, Morocco

46

47 **Résumé**

48 Les variations de la susceptibilité magnétique (SM) sont généralement attribuées à
49 des changements eustatiques et/ou climatiques qui ont un impact sur l'apport des
50 minéraux magnétiques détritiques. Cependant, le mécanisme responsable de
51 l'apport de minéraux magnétiques du continent vers l'océan n'est pas entièrement
52 compris. La minéralogie de roche totale, la méthode de Rietveld à partir de
53 diffractogrammes de poudres et la géochimie de roche totale, combinés à une étude
54 de SM sur une séquence sédimentaire du Crétacé supérieur/Paléogène d'une
55 épaisseur de ~290 m à Erguïta, au Maroc, impliquent que le fer a une origine
56 exclusivement détritique. Les fluctuations de la SM se sont produites
57 indépendamment du cadre environnemental de dépôt et des variations du niveau de
58 la mer. Les études sur le magnétisme des roches montrent qu'un assemblage
59 complexe de minéraux ferromagnétiques *sensu lato* est enregistré dans la section
60 sédimentaire d'Erguïta, et que de la magnétite plus ou moins oxydée contrôle les
61 variations de susceptibilité magnétique. Cette étude montre que l'altération
62 probablement du socle cristallin de l'Anti-Atlas a entraîné l'apport de phyllosilicates
63 détritiques contenant du fer et d'oxydes de fer ferromagnétiques (*sensu lato*) vers la
64 marge passive orientale de l'océan Atlantique, de la fin du Crétacé jusqu'au milieu du
65 Paléogène. L'intensité accrue de l'altération a entraîné une augmentation du matériel
66 magnétique détritique dans toutes les lithologies, ce qui, à son tour, a augmenté le
67 signal de SM. Il est important de noter que ce modèle coïncide parfaitement avec les
68 bouleversements climatiques du Paléogène. Nous proposons que ce lien méconnu
69 entre la SM et l'intensité de l'altération induite par le climat soit primordial pour
70 élucider l'origine de l'intervalle à faibles valeurs de SM sous la limite Crétacé-
71 Paléogène. Un refroidissement climatique entraînant une réduction de l'altération
72 plutôt qu'une acidification globale déclenchée par la phase 2 du volcanisme du
73 Deccan pourrait contribuer à expliquer la tendance à la SM à cette époque.

74

75 Mots clés : Susceptibilité magnétique, altération, climat, Crétacé/Paléogène, Erguïta,
76 Maroc

77

78 **1. Introduction**

79 The magnetic susceptibility (MS) has been recently invoked as a proxy to identify the
80 Cretaceous-Paleogene (K-Pg) transition (e.g., Abrajevitch et al., 2015; Font et al.,
81 2011; Lowrie et al., 1990). In principle, better constraints on the relationships
82 between MS and climatic and environmental changes could improve our
83 understanding of the external factors controlling the MS record.

84 MS, which quantifies the capacity of a material to be magnetized in the
85 presence of a magnetic field, first allows assessing the proportion of detrital-
86 dominated ferromagnetic *sensu lato* (iron oxides), paramagnetic (e.g., Fe-bearing
87 silicates and most of the iron sulfides), and diamagnetic (e.g., iron-free carbonates
88 and quartz) minerals in a given sediment (Ellwood et al., 2000; Riquier et al., 2010).
89 The mineralogical nature of Fe-oxides strongly impacts the MS values (Da Silva et
90 al., 2015). Although paramagnetic and diamagnetic minerals show very low positive
91 or negative MS values, respectively (Ellwood et al., 2000), variations in MS, together
92 with detailed rock magnetic analyses, have been linked to changes in ferromagnetic
93 contribution (Pas et al., 2019; Riquier et al., 2010). Moreover, magnetic minerals with
94 a high coercivity such as hematite yield lower MS signals compared to magnetite, a
95 low coercivity mineral (Da Silva et al., 2013). In sedimentary environments, the
96 primary MS signal is linked to detrital minerals and can be altered by the formation of
97 secondary minerals during diagenesis and metamorphism alteration (Ellwood et al.,
98 2000). Thus, post-depositional processes must be screened for potential modification
99 of the primary MS signature.

100 MS has been increasingly used to assess the amount of detrital inputs in
101 conjunction with sea level changes, leading to the idea that MS could constitute an
102 independent proxy to document several millions of years of long-term trends of
103 eustatic changes (Da Silva et al., 2015, 2010, 2009; Hladil, 2002; Mahboubi et al.,
104 2019). High MS values were hypothesized to reflect an increasing detrital supply
105 related to sea level fall, particularly in the Frasnian-Famennian transition, where
106 major extinctions coincided with profound eustatic fluctuations (Averbuch et al., 2005;
107 Girard et al., 2021; Riquier et al., 2010). It was supported that MS and sea-level
108 change only covary for a short period of thousands of years (Boulila et al., 2010;
109 Whalen and Day, 2010). Yet, it remains unclear how depositional environments
110 (proximal versus distal) at a given stratigraphic level influenced the MS record.

111 Several studies have proposed that MS is a correlation tool and generally
112 records paleoclimatic variations (influencing or not eustasy) in sedimentary rocks
113 (Boulila et al., 2010, 2008; Da Silva et al., 2015; Ellwood et al., 2000; Font et al.,
114 2011; Mead et al., 1986; Nowaczyk et al., 2002; Pas et al., 2019; Stage, 2001;
115 Vanderaveroet et al., 1999; Whalen and Day, 2010; Wouters et al., 2019). This
116 inference comes from the relationship between MS trends and oxygen isotopes in
117 Pleistocene sections (Robinson, 1986) and astronomically-driven Milankovitch cycles
118 in Devonian and Jurassic sequences (Boulila et al., 2010; Da Silva et al., 2020, 2015;
119 Ellwood et al., 2015). However, the mechanism that leads to the covariation between
120 climatic variations and MS remains poorly understood.

121 Here, we explore the MS signal of a ~290 m-thick Upper
122 Cretaceous/Paleogene phosphorus (P)-bearing sedimentary sequence at Erguita in
123 the Moroccan western High Atlas (WHA), where the sequence stratigraphic
124 framework is well-established (El Bamiki et al., 2020). We use a combination of
125 mineralogical, rock magnetism, and geochemical techniques to demonstrate the
126 detrital origin of MS signal across the section. Then, we provide evidence linking MS
127 variations to climate-driven weathering intensity. The findings also offer new insights
128 on using MS records in deep geological time.

129

130 **2. Geological background**

131 2.1. General information

132 The ENE-trending High Atlas Mountain belt in Morocco belongs to the Atlas system
133 that spreads over thousands of kilometers from the Atlantic coast to Tunisia. The
134 tectonic convergence between the African and Eurasian plates since the Late
135 Cretaceous has promoted the inversion of the Mesozoic-Cenozoic intracontinental
136 basin (Atlasic basin) during which former syn-rift faults were reactivated (Frizon de
137 Lamotte et al., 2008; Michard et al., 2008).

138 The Triassic Central Atlantic rifting initiated the formation of the Atlasic basin in
139 Morocco, which resulted in important thermal subsidence and subsequent deposition
140 of km-thick Mesozoic marine sequences near the rifted zones (Ellouz et al., 2003).
141 This is in contrast to the thin Upper Cretaceous-Paleogene sedimentary successions
142 that were formed when thermally-induced subsidence stopped at the initiation of the
143 Africa-Eurasia convergence (Ellouz et al., 2003). In Morocco, a tremendous amount
144 of phosphate-rich sediments accumulated on shallow water platforms under the

145 strong influence of Atlantic upwelling currents from the Late Cretaceous to the
146 Eocene (Pufahl and Groat, 2017). They are now preserved within vast plateaus (e.g.,
147 Gantour, Ouled Abdoun, and Meskala basins) and along the margins of the western
148 High Atlas (Fig. 1a). The P-rich sediments were bordered by the deformed Variscan
149 basement to the north and east, and by the Paleozoic fold belt of the Anti-Atlas to the
150 south (Herbig and Trappe, 1994). The latter constituted the adjacent hinterland area
151 (El Bamiki et al., 2020). Then, the WHA recorded multiple phases of shortening and
152 uplift with a major event during the Neogene (Frizon de Lamotte et al., 2008, 2009;
153 Lanari et al., 2020; Leprêtre et al., 2018; Missenard et al., 2008). The erosion of the
154 uprising WHA is delivering substantial continental materials to foreland basins (i.e.,
155 Haouz, Ouarzazate, and Souss basins), which formed along the northern and
156 southern margins of the orogen (Michard et al., 2008).

157

158 2.2. Erguita section

159 The Erguita section described by Ambroggi in the sixties corresponds to the distal
160 facies of the WHA sedimentary sequences (Ambroggi, 1963). In contrast, shallow
161 proximal facies are found to the east in the Ouarzazate basin (Fig. 1a) (El Bamiki et
162 al., 2020). The phosphate-bearing series, first deposited during the Maastrichtian,
163 unconformably overlies Campanian carbonates (Ambroggi, 1963). Based on
164 sedimentological features, sequence stratigraphy, and biostratigraphic data of
165 nannoflora, second-order transgressive-regressive cycles have been successfully
166 described in the WHA between the Late Cretaceous and Eocene (El Bamiki et al.,
167 2020). The Maastrichtian Erguita rocks, consisting of marls and P-poor carbonates
168 accumulated during an episode of sea level rise and fall, are capped by thin gypsum
169 layers (Figs. 1b, c, 2a) (El Bamiki et al., 2020). The large regression of the late
170 Maastrichtian, leading to the widespread karstification in the eastern part of the WHA
171 has been inferred as the potential event that facilitates gypsum precipitation in
172 proximal environments at Erguita. The overlying Danian-Selandian rocks are mainly
173 characterized by P-rich calcarenites, marls, and thin P-poor carbonated sandstones
174 passing upwards through massive P-rich carbonated sandstones (Figs. 1b, c, 2b) (El
175 Bamiki et al., 2020). In these sediments, hummocky cross-stratification, interpreted to
176 form within the outer platform between the storm wave-base and the fair-weather
177 wave-base (Burchette and Wright, 1992), and overlying gravity-flow deposits,
178 accumulated below the storm wave-base, indicate a basin deepening (Figs. 1b, 2c,

179 d) (El Bamiki et al., 2020). Deposition of organic-rich marls in the Erguita section has
180 recorded the maximum flooding interval, a stratigraphic marker interval in the WHA
181 (Fig. 1b) (El Bamiki et al., 2020). Then, the basal Thanetian sediments are dominated
182 by turbiditic phosphates, where the phosphatic particles have been transported
183 basinward and rapidly accumulated with a normal grading pattern (Fig. 1b, c) (El
184 Bamiki et al., 2020). The greater distance of the Erguita depositional setting from the
185 phosphogenic window and larger detrital inputs diluting phosphate concentrations
186 have led to lower phosphorus enrichment in sediments compared to the Gantour
187 basin, among others (Aubineau et al., 2024a; El Bamiki et al., 2020, 2021, 2023).
188 The progressive deposition of P-containing calcarenites and carbonates, clayey
189 calcarenites, shell beds, and marls, together with the upward increase in faunal
190 content (nautiloids, *Thalassinoides* burrows network, gastropods, bivalves, oysters),
191 characterize the upper part of the section (Figs. 1b, c, 2e-i) (El Bamiki et al., 2020).
192 This pattern reflects the regressive phase of the basin, where macroorganisms were
193 likely diversified during the Eocene. During the studied interval, detrital materials and
194 soluble elements probably originated from the emerged Anti-Atlas rocks (El Bamiki et
195 al., 2020; Herbig and Trappe, 1994). Finally, this section is truncated and
196 unconformably covered by Neogene conglomeratic sediments resulting from the
197 erosion of the uprising High Atlas (Ambroggi, 1963; El Bamiki et al., 2020).

198

199 **3. Material and methods**

200 3.1. Sampling and sample preparation

201 We sampled 279 oriented cylindrical cores with a portable gasoline-powered rock
202 drill, three oriented blocks with hand sampling techniques (Tauxe et al., 1998), and
203 additional unoriented rocks from the Erguita section in Morocco. All samples from
204 freshly exposed outcrops are in the vicinity of the Erguita riverbed. The coordinates
205 are presented in Table S1. A hundred of stratigraphic levels were studied within the
206 ~290 m thick sedimentary section to characterize the magnetic susceptibility (Fig.
207 1b). The sampling interval ranges from 0.5 to 6.8 m.

208 In each of the drilled horizon, three oriented cylindrical cores were collected.
209 The drilling of oriented blocks was carried out at Geosciences Montpellier, University
210 of Montpellier. For clarity, sample “1” refers to cylindrical cores number 1, 2, and 3,
211 while “OB” refers to the oriented blocks. We designated unoriented rocks with a letter

212 behind the sample number. For example, sample 109a is therefore located between
213 oriented samples 109 and 112.

214 We constructed the lithostratigraphic column after carefully examining
215 outcrops, cylindrical cores, the gamma-ray curve, and XRD and geochemical data
216 (Fig. 1b, c). We logged all samples to provide information on their stratigraphic
217 position. Standard specimens (2.2 cm in height and 2.5 cm in diameter) from the
218 oriented cylindrical cores and oriented blocks (1 to 5 per core) were prepared at
219 Geosciences Montpellier, leading to the production of more than 800 specimens.
220 From those cylindrical specimens, 636 were selected (specimens that did not fit into
221 the 3D rotator sample holder were not analyzed) and measured to study the
222 magnetic susceptibility. We crushed and milled by hand in agate mortar
223 representative samples for mineralogical and whole-rock geochemical examination.
224

225 3.2. X-Ray Diffraction

226 X-ray diffraction (XRD) mineral analyses were performed on powdered bulk
227 samples using a Bruker D8 ADVANCE diffractometer (CuK α radiation) operating at
228 40 kV and 40 mA to identify the mineralogical phases of P-containing rocks at RRXG
229 platform, University of Montpellier. Analysis of bulk powders was performed over an
230 angular range of 4–62° 2 θ and a step size of 0.02° 2 θ per 2 s. Bruker Eva software
231 was used for indexing peaks, and XRD patterns were compared with reference data
232 (Brindley and Brown, 1980).

233 Moreover, Rietveld refinement of XRD patterns allowed a semi-quantification
234 of bulk mineralogy (Table 1) using the Profex 4.3.1 interface with the program BGMN
235 (Döbelin and Kleeberg, 2015). Regardless of the software programs used,
236 quantification is challenging when dealing with clay minerals (Hillier, 2000). The
237 accuracy of clay mineral quantification is generally lower than 5 wt.% and up to 10
238 wt.% when amorphous phases are present (Warr, 2022).

240 3.3. Whole-rock geochemistry and weathering intensity

241 We performed whole-rock geochemical analyses of major and trace elements on 10
242 samples of various lithologies (Table 2). Powdered samples were fused with lithium
243 metaborate (LiBO₂) for trace and major element measurements (Carignan et al.,
244 2001). Major elements were measured by inductively coupled plasma (ICP) optical
245 emission spectrometry, and trace elements by ICP mass spectrometry at Service

246 d'Analyse des Roches et Minéraux, Nancy, France. Measurement uncertainty and
247 instrument detection limit relative to international standards and sample replicates
248 (Carignan et al., 2001) are provided in Table S2. Reference standards include Basalt
249 BR, anorthosite AN-G, diorite DR-N, serpentinite UB-N, and granite GH (Carignan et
250 al., 2001).

251 The quantification of the degree of chemical weathering of source rocks was
252 determined by means of the chemical index of alteration (CIA), where $CIA =$
253 $[Al_2O_3 / (Al_2O_3 + CaO^* + Na_2O + K_2O) \times 100]$ in mole fraction (Nesbitt and Young, 1982).
254 CaO^* is the amount in the silicate fraction. Considering the varying proportions of
255 carbonates and phosphates in the Erguita sedimentary rocks (see section 4.2), CaO^*
256 of our samples is assumed with $CaO^* = CaO$ when the mole fraction of CaO is \leq
257 Na_2O and $CaO^* = Na_2O$ when the mole fraction of CaO is $\geq Na_2O$, as previously
258 reported (Jian et al., 2013). Typically, unweathered, moderately weathered, and
259 highly weathered rocks have low (<60), 60-80, and high (>80) CIA values,
260 respectively (Fedo et al., 1995). The pristine phosphatic lithofacies usually show low
261 P_2O_5 contents, while substantial P enrichment within sediments derives from
262 syndepositional repetitive wave and storm winnowing by removing the fine-grained
263 sedimentary detritus (Pufahl and Groat, 2017). As a result, the formation of
264 winnowed phosphates (i.e., phosphate-rich rocks) hinders the calculation of CIA due
265 to potential removal of the silicate fraction (Table 2).

266

267 3.4. *In situ* gamma-ray spectrometry

268 Uranium concentrations, used as a proxy for sedimentary phosphate minerals, were
269 measured *in situ* with a portable gamma-ray spectrometer: the Gamma Surveyor
270 Vario (GF Instruments), equipped with a Bismuth Germanium Oxide
271 (BGO; $Bi_4Ge_3O_{12}$) scintillator with 2048 channels, along with a 19 cm^3 detector with
272 probe dimensions of 45 mm and a length of 301 mm (VB1). This equipment allows
273 the measurement of energies up to 3 MeV. In all studied stratigraphic levels,
274 measurements were acquired by direct probe contact with rock outcrops at planar
275 spots (Table S3). The measurement time was 180 seconds, as recommended by the
276 manufacturer to optimize time and precision.

277

278 3.5. Magnetic measurements

279 Magnetic susceptibility measurements were performed on 640 specimens using an
280 AGICO KLY-5 Kappabridge with an alternative field of $400 \text{ A}\cdot\text{m}^{-1}$ peak value
281 (frequency: 1220 Hz) at the *Géosciences Environnement Toulouse* laboratory
282 (France). We normalized the MS values with respect to the theoretical volume of
283 specimens (10 cm^3). Anisotropy data were processed with the ANISOFT software
284 v.6.1.01 (Chadima and Jelínek, 2008). The ellipsoid of magnetic susceptibility is
285 defined by the orientation and length of the three principal susceptibility axes with
286 $K_1 > K_2 > K_3$ (Jelinek, 1981). K_m represents the mean volume-specific magnetic
287 susceptibility (SI) and reflects the volume content of magnetic minerals in the
288 specimen. The degree of anisotropy ($P = K_1/K_3$) represents the intensity of the
289 preferred orientation of magnetic minerals. The T parameter represents the shape of
290 the ellipsoid and varies from -1 (perfectly prolate) to +1 (perfectly oblate). The
291 magnetic lineation ($L = K_1/K_2$) is defined by the maximum axis of the ellipsoid, and
292 the magnetic foliation ($F = K_2/K_3$) is the plane containing K_1 and K_2 .

293

294 3.6. Rock magnetism investigations

295 Carbonates and carbonated sandstones from the Erguita section carry natural
296 remanent magnetizations with values ranging from 1.8×10^{-10} to $1.9 \times 10^{-09} \text{ Am}^2$
297 (measurements from 79 oriented core specimens using the Sushibar at LMU
298 Munich). Such rocks with both weak magnetization and weak magnetic susceptibility
299 values (see Results) are challenging to accurately characterize the magnetic
300 mineralogy by means of standard techniques. To tentatively define the magnetic
301 mineralogy, we measured the magnetic hysteresis of six selected samples at room
302 temperature and the low-temperature remanence with a sensitive Quantum Design
303 Magnetic Properties Measurement System (MPMS 3) at the Institute Charles
304 Gerhardt Montpellier (France). The samples were selected along the section to
305 represent stratigraphic levels with strong, intermediate, and weak magnetic
306 susceptibility values. We used the SQUID-VSM configuration of the MPMS3 to
307 achieve a sensitivity, which is lower than $1 \times 10^{-11} \text{ Am}^2$. The bulk fragments were
308 mounted on a clean quartz paddle holder with varnish (sample mass $< 50 \text{ mg}$ and
309 maximum magnetic moments of the quartz rode measured at room temperature with
310 2.5 T : $5.6 \times 10^{-10} \text{ Am}^2$). Hysteresis curves were measured at room temperature
311 between -1 and 1 Tesla and processed with HystLab (Paterson et al., 2018). We
312 performed the following low temperature characterization protocol (FC-ZFC-

313 RTSIRMcool-RTSIRMwarm) for the 6 samples (Bilardello and Jackson, 2013): (i) we
314 applied a 2.5 T field during the cooling of the sample followed by the measurement of
315 the remanence until 300 K in zero field (FC, Field-Cooled curve); (ii) next the sample
316 is Zero-Field Cooled and the remanence is measured after applying a short 2.5 T
317 field at low temperatures (ZFC curve); (iii) then, we applied a 2.5 T field at room
318 temperature and we measured the remanence (Room Temperature Saturation
319 Isothermal Remanent Magnetization, RT-SIRM) during the cooling (RT-SIRMcool)
320 and warming to 300 K (RT-SIRMwarm).

321

322 **4. Results**

323 4.1. Rock magnetism results

324 At first glance and considering the complexity of measuring rock magnetic data of
325 these rocks, three groups of magnetic mineralogy were determined (see Figure S2
326 for the extensive dataset). The first group (including samples 28, 109, and 166
327 among the six selected samples) is characterized by samples with a sharp Verwey
328 Transition (T_v) observed at ~ 120 K (Kosterov, 2002; Özdemir et al., 2002; Verwey,
329 1935) in both ZFC and RT-SIRM curves, indicating the presence of magnetite as the
330 dominant carrier of the remanent magnetization (Fig. 3a). Moreover, the ZFC curve is
331 above the FC curve, which could suggest a dominance of monodomain grains even if
332 we cannot exclude the presence of pseudo-single domain grains. Indeed, the M_{rs}/M_s
333 ratios (ratio of remanent saturation moment M_{rs} to saturation moment M_s) derived
334 from room temperature hysteresis curves show values between 0.08 and 0.12,
335 suggesting a possible pseudo-single domain state rather than single-domain state
336 (Dunlop and Özdemir, 1997). We observe a hump-shaped in the cooling curves
337 between 300 K and the Verwey transition associated to a symmetric hump in the
338 warming curve, which could be associated to the maghemitization, i.e., the partial
339 oxidation of the magnetite particles (Özdemir and Dunlop, 2010). Finally,
340 convergence of FC and ZFC curves around 300 K (Fig. S2) could suggest the
341 presence of goethite in these samples (Taylor et al., 2014). The second group
342 (samples 1 and 103) reveals a faint T_v in the ZFC curve due to magnetite with a
343 downward curvature for the RT-SIRM curves (Fig. 3b). For the sample 103, the
344 magnetic grains seem to be in a superparamagnetic state with no observed coercivity
345 associated to a large remanence drop below 50 K (FC curve). Such smooth and
346 broadened T_v can also be associated to the presence of maghemite. This is

347 consistent with the hypothesis that the finest particles are the most affected by the
348 maghemitization (Özdemir and Dunlop, 2010). Presence of goethite is also
349 suggested by the FC-ZFC convergence after 250 K. The third group (only sample
350 250) is dominated by the presence of goethite with a characteristic behavior of the
351 reversible RT-SIRM, ZFC, and FC curves (Fig. 3c) (Dekkers, 1989). A faint T_v is
352 observed in this sample when looking at the ZFC derivative curve (Fig. S2). The
353 nearly straight with a slight opened loop of the hysteresis curve supports the occurrence
354 of magnetite together with a mixture in the magnetic assemblage (Fig. 3c). It is worth
355 noting that the presence of other iron oxide minerals (e.g., hematite) or pyrrhotite
356 cannot be ruled out with the available data. For example, a small peak at ~250 K for
357 RT-SIRM cool for samples 28 and 166 is observed, but the Morin transition,
358 indicating the presence of hematite (Morin, 1950; Özdemir and Dunlop, 2005), is not
359 supported on the ZFC/FC curves (Fig. S2). Collectively, these rock magnetic data
360 demonstrate the presence of dominant paramagnetic phase as suggested by a steep
361 positive slope of the hysteresis loops associated with a complex ferromagnetic *sensu*
362 *lato* assemblage with fine magnetite that can be altered in maghemite, and goethite.
363 Presence of pyrrhotite or hematite is not excluded.

364

365 4.2. Magnetic susceptibility data and weathering intensity

366 Depending on the lithology and the number of specimens (3 to 13 per horizon), 2 to
367 10 measures from different specimens were performed and averaged for each
368 stratigraphic level (Table S4). The P-containing samples studied along the
369 stratigraphic interval of the Erguita section have a mean MS range of $-6.2 \cdot 10^{-6}$ to
370 $6.8 \cdot 10^{-5}$ SI (Fig. 4a). Moving upsection, the MS values first show a general increase
371 of $3.1 \cdot 10^{-5}$ SI between samples 1 and 28. This is then followed by a progressive
372 upward decrease from the samples 28 to 184, with mean MS values spanning $5.5 \cdot 10^{-5}$
373 5 to $-3.3 \cdot 10^{-6}$ SI, before increasing and decreasing again to $2.6 \cdot 10^{-5}$ SI (sample 250)
374 and $-3.1 \cdot 10^{-6}$ (sample 277), respectively. Also, multiple short-term MS fluctuations
375 are observed within these intervals. Finally, the MS values switch to a dramatic
376 ascending increase in sample OB3 with $6.8 \cdot 10^{-5}$ SI. Importantly, the MS trends do not
377 vary in response to lithological or long-term eustatic changes. On the other hand, a
378 notable positive relationship is observed between MS and CIA values, as evidenced
379 by an R^2 value of 0.6 and a p-value of 0.02 (Fig. 4b). The average CIA value in the

380 studied section is 68 ± 7 , suggesting a moderate level of weathering in the source
381 rocks (Fedo et al., 1995; Nesbitt and Young, 1982).

382

383 4.3. Relationships between MS and mineralogical and geochemical contents

384 Before evaluating the influence of detrital input on MS, we constrained and semi-
385 quantified the mineralogical phases of 27 samples of various lithologies (Fig. S1,
386 Table 1). Bulk XRD mineralogical data show that the Erguita sediments mainly
387 comprise two dolomitic minerals and quartz with varying proportions of calcite,
388 carbonate fluorapatite (CFA), and clay minerals. K-feldspars, gypsum, and pyrite
389 appear in small abundances. Typical clay minerals like chlorite, illite/mica, smectite,
390 and kaolinite are observed. In addition, palygorskite, which is a Si- and Mg-rich
391 phyllosilicate (Brindley and Brown, 1980), was mainly detected in the lowermost and
392 uppermost parts of the section (Fig. S1), where the sedimentary succession displays
393 very shallow-water environments. The clay mineralogical assemblage at Erguita is
394 closely similar to the Gantour and WHA lithologies (Aubineau et al., 2022a, 2022b).
395 In general, the XRD mineralogical analysis reveals that siliciclastic detrital material is
396 widespread throughout all lithologies, except two pure carbonate samples.

397 There is no significant correlation between the proportions of carbonates,
398 quartz, and CFA and the evolution of MS ($R^2 = 0.02$, $p = 0.57$ for carbonates, $R^2 =$
399 0.01 , $p = 0.72$ for quartz, and $R^2 = 0.2$, $p = 0.04$ for CFA). However, the scatter plot
400 between the amount of clay minerals and MS reveals a strong covariation ($R^2 = 0.72$,
401 $p = 0.22$) (Fig. 5). This is coherent with the strong covariation between Al – a detrital
402 indicator – and MS ($R^2 = 0.76$, $p = 0.001$) (Fig. 6a). In addition, the Fe *versus* MS plot
403 indicates that the origin of the MS signal is well supported by Fe-bearing minerals (R^2
404 $= 0.87$, $p = 7.10^{-5}$) (Fig. 6b). The near-perfect covariation between Al and Fe ($R^2 =$
405 0.95 , $p = 2.10^{-6}$) points to a detrital origin of Fe-bearing minerals (Fig. 6c). Although
406 zircons are presumably detrital grains, the lack of correlation between Zr and MS (R^2
407 $= 0$, $p = 0.90$) suggests that zircons and magnetic grains were not tightly bound
408 during transportation and deposition of the Erguita sediments (Fig. 6d), which is best
409 explained by their difference in grain size and density.

410 The PAAS-normalized Rare Earth Element and Yttrium ($REEY_{SN}$, where SN
411 represents values normalized to PAAS) patterns of the Erguita sediments are
412 relatively similar to each other (Fig. 7a), suggesting uptake of REEY from a
413 geochemically uniform fluid. The $REEY_{SN}$ patterns show light (L)REE depletions

414 relative to heavy (H)REE with $(La/Yb)_{SN}$ values ranging from 0.49 and 0.88 (Fig. 7a;
415 Table 2). The latter observation is consistent with the $(Sm/Yb)_{SN}$ and $(Sm/Pr)_{SN}$ ratios
416 plotting on the HREE enriched field (Fig. 7b), excluding middle (M)REE enrichment.
417 Moreover, the $(Ce/Ce^*)_{SN}$ versus $(Pr/Pr^*)_{SN}$ diagram reveals a true negative Ce
418 anomalies in the Erguita sediments (Fig. 7c). Combined, these characteristics yield
419 features akin to those of modern seawater (Alibo and Nozaki, 1999; Bau et al., 1997;
420 Bau and Dulski, 1996; De Baar et al., 1985; Garnit et al., 2012). Besides, the
421 sediments have Y/Ho ratios between 26 and 46, reflecting terrestrial and marine
422 mixing inputs, where Y/Ho ratios >40 and ~ 26 represent a seawater signal and a
423 strong terrestrial input dominated by fine-grained materials, respectively (Bau et al.,
424 1997). This is further supported by the strong covariation between Y/Ho and Zr in the
425 carbonated sandstones ($R^2 = 0.72$) (Fig. 7d).

426

427 **5. Discussion**

428 5.1. Diagenetic considerations

429 Post-depositional processes during diagenesis can alter the primary MS signature.
430 For example, Schneider et al. (2004) suggested a genetic link between MS values
431 and Fe-rich carbonates formed during the migration of diagenetic fluids. Although the
432 Erguita limestones are dolomitized, numerous lines of mineralogical and geochemical
433 evidence point to an absence of late'/extensive diagenetic processes that could have
434 erased the detrital MS signal.

435 Sediments fed by hydrothermal fluids are usually enriched in Fe (e.g.,
436 Chavagnac et al., 2018; Clarkson et al., 2014), leading to an absence of covariation
437 between Al and Fe. No such decoupling was observed in the Erguita sediments.
438 Instead, the strong correlations between Al, Fe, and MS reflect the detrital
439 prevalence of magnetic minerals. Bulk XRD patterns do not show illite/smectite
440 mixed-layer minerals. The absence of such minerals in other WHA sections
441 (Aubineau et al., 2022a; Knidiri et al., 2014) indicates minimal diagenetic
442 transformations within the sediment pile (Środoń and Eberl, 1984; Velde et al., 1986).
443 Besides, elevated CFA-hosted CO_3^{2-} concentrations characterize the P-containing
444 Erguita samples, where they averaged 5.9 ± 1.6 (1σ , $n = 13$) (Table S5, method of
445 calculation presented in Schuffert et al. (1990), comparable to the 4-8 wt.% CO_3^{2-}
446 content of Moroccan CFA grains (Aubineau et al., 2024b, 2022b, 2022a; Cosmidis et
447 al., 2013; El Bamiki et al., 2023; Kocsis et al., 2014; Nguidi et al., 2021). This trend

448 results from the equilibrium of CFA with seawater (Nathan, 1984), while thermal
449 diagenesis and weathering result in progressive decarbonation of CFA toward
450 fluorapatite composition (i.e., nearly zero CO_3^{2-} substitution) (McClellan and Van
451 Kauwenbergh, 1991).

452 Furthermore, the REEY distribution in sedimentary rocks allows the evaluation
453 of seawater chemistry in depositional settings. REEY typically exhibit a conservative
454 behavior (i.e., no fractionation) during sediment deposition (e.g., Bau and Dulski,
455 1996; Shields and Stille, 2001). The REEY pattern and composition in the Erguita
456 sediments agree with deposition in fully oxygenated seawater (Alibo and Nozaki,
457 1999; Bau et al., 1997; Bau and Dulski, 1996; De Baar et al., 1985). MREE
458 enrichment with respect to LREE and HREE (Reynard et al., 1999), caused by
459 anoxic porewaters or late diagenetic fluids as a source of REEY is not observed in
460 our samples. The $(\text{La}/\text{Yb})_{\text{SN}}$ ratios ranging from 0.5 to 0.9 in the Erguita sediments
461 compared to 0.4-0.5 for modern seawater suggest adsorption mechanisms (Reynard
462 et al., 1999). The negative correlation between Zr and Y/Ho, together with Y/Ho
463 ratios being more similar to clastic sediment values, hint that REEY values are also
464 influenced by siliciclastic detritus derived from continental weathering. Therefore, we
465 interpret the REEY distribution at Erguita to mirror the chemical composition of
466 seawater, from which terrestrial REEY fluxes via continental runoff were sourced to
467 the depositional environments. Also, the REEY probably adsorbed onto the
468 siliciclastic detritus.

469 In light of the above considerations, the MS signal in this study is primarily
470 attributed to detrital sources. Thus, the Erguita MS data can be reliably used for
471 paleoenvironmental and/or paleoclimatic reconstructions.

472

473 5.2. Origin of the magnetic susceptibility variations

474 The rock magnetism of representative Erguita rocks has revealed that there is no
475 correlation between the magnetic mineralogy and variations in magnetic susceptibility
476 since the magnetite-bearing samples of the first group show both high and low MS
477 values. The MS signal at Erguita does not correspond to the lithological changes, but
478 instead shows a consistent relationship with the amount of clay mineral present in the
479 entire section. The MS changes could be attributed to variations of paramagnetic
480 mineral proportions, such as Fe-bearing phyllosilicates. However, the dominant
481 presence of Fe-free palygorskite $[\text{Si}_8\text{O}_{20}(\text{Mg}_2\text{Al}_2)(\text{OH})_2(\text{OH}_2)_4 \cdot 4\text{H}_2\text{O}]$ (Singer and

482 Galan, 1984) associated with the highest MS value in the upper part of the section
483 does not fully support the relationship between MS and paramagnetic mineral
484 content. Collectively, the data suggest that the proportion of more or less oxidized
485 magnetite supplied to the depositional setting controls the MS variations at Erguita.

486 The covariation between MS and clay mineral content likely indicates that
487 ferromagnetic *sensu lato* minerals and phyllosilicates were supplied together to the
488 depositional setting. The Erguita samples show a magnetic fabric typical of
489 sedimentary rocks (type 1 according to Aubourg et al., 2004), which is revealed by
490 the high inclination of K3 axes and the random distribution of K1 and K2 axes within
491 the horizontal plane (Fig. 8a). Figure 8 shows that the magnetic foliation of the mean
492 average of all sites from the Erguita section is oblique to the bedding plane by $\sim 24^\circ$,
493 whereas the K1 axis is perpendicular to the K3 direction. At first order, there is an
494 overall consistency across the ~ 290 m-thick section. Such AMS fabric suggest that
495 the particles are rolled and transported from the SE to the NW if we assume the K3
496 axis as an indicator of paleocurrent direction. A site-by-site analysis shows a
497 tendency with a predominance of oblate-type ellipsoid when the fabric is very well
498 defined. The main AMS fabric may reflect the behavior of the different paramagnetic
499 phases in the samples, as suggested by the rock magnetic data (Fig. S2). Moreover,
500 for the specimens dominated by a ferromagnetic *sensu lato* assemblage (e.g.,
501 sample 166), the corresponding AMS may reflect the behavior of oxidized magnetite
502 associated to goethite particles. The samples were further divided into two
503 subpopulations, representing the phyllosilicate proportion (Fig. S3). The Al-rich
504 samples (i.e., high proportion of clay minerals) show a more oblate fabric parallel to
505 the bedding plane in agreement with the platy morphologies of the phyllosilicates
506 compared to the Al-poor samples (i.e., low proportion of clay minerals). The K3 axis
507 for the Al-rich samples are plunging to the N with a slight imbrication. After removing
508 the specimen with high-anisotropy value (ERA31A), the fabric of the Al-poor samples
509 is better defined with a fabric close to the Al-rich subpopulation with an imbrication to
510 the NW. Despite a wide dispersion, the K1 is relatively aligned to the K3 direction.
511 Given the lack of sedimentary evidence to provide a paleocurrent orientation, the
512 dominant direction of the K3 axes to the NW could be used as a first indicator.

513 We hypothesize the emerged Anti-Atlas crystalline basement to the SE as a
514 source of detrital materials to the Erguita depositional environment, as already
515 suggested by El Bamiki et al. (2020) and Herbig and Trappe (1994). Thus, one

516 process occurring on the Anti-Atlas Mountains should exclusively explain the
517 simultaneous delivery of clay and ferromagnetic minerals to the depositional sites.
518 Some sites (52, 100, 229, 247, 250) show an inverse fabric with horizontal K3 in Fig.
519 8. The hypotheses to explain the origin of such inverse AMS fabric include the
520 occurrence of (i) single-domain magnetite (Potter and Stephenson, 1988), (ii) high
521 susceptibility minerals as maghemite (Borradaile and Puumala, 1989), (iii) greigite
522 and some suitable titanomagnetite compositions (Aubourg and Robion, 2002).

523 Autocyclic physical processes, including tidal current and wave and storm
524 winnowing, are superimposed on tectono-eustatic-climatic allocyclic forcing (Walker
525 and James, 1992). Inherent to the depositional system, the former processes over
526 short-time and temporal scales may reduce the visibility of the expected long-term
527 allocyclic variations. With this in mind, hydrodynamic winnowing, reworking, and
528 transporting that have led to the in-situ phosphate enrichment in the Erguita
529 sediments (El Bamiki et al., 2020) may have been an important controlling factor.
530 These hydrodynamic processes could have thus removed the ferromagnetic and
531 paramagnetic fractions, increasing and decreasing the CFA content and MS values,
532 respectively. In the Moroccan phosphate-bearing rocks, uranium is mainly hosted by
533 CFA (Aubineau et al., 2022a). In addition to U, P_2O_5 concentration is a tracer for CFA
534 enrichment. Combined, these proxies allow to decipher whether the autocyclic
535 processes led to the observed MS variations in the Erguita section. The relationships
536 between CFA abundance, U and P_2O_5 concentrations, and associated MS are weak,
537 as shown in Figure 5 and Figure S4. This strongly supports that mechanical
538 winnowing/reworking, resulting in the phosphate enrichment in sedimentary
539 environments, along the Atlantic Paleogene passive margin did not intensively
540 contribute to the expression of MS values.

541 Weathering drives the delivery of siliciclastic material from the land to oceans
542 (Walker et al., 1981). Global tectonic, sea-level, and climate changes strongly
543 influence weathering regimes. Thus, such events should exert considerable pressure
544 on the flux of magnetic minerals. Considering the relative tectonic stability in
545 northwestern Morocco between the late Cretaceous and Paleogene (Charton et al.,
546 2021), the onset of the Africa-Eurasia convergence did not influence the MS values.
547 The amount of detrital particles transported from land to oceans could have
548 increased during times of regression (Crick et al., 1997; Ellwood et al., 1999). In this
549 scenario, sea level fall leads to a lowering of the base level, which in turn increases

550 erosion. However, our results show a long-term decreasing MS trend in both sea
551 level rise and fall, hinting that eustatic fluctuations over millions of years did not
552 influence the MS trend in the Erguita section.

553 In contrast, MS values correlate well with CIA – a proxy of weathering
554 intensity, suggesting a direct connection between climate change and MS.
555 Nonetheless, the CIA values of sedimentary rocks may be prone to unavoidable
556 limitations (Fedo and Babechuk, 2022; Meunier et al., 2013). Besides, the omission
557 of SiO₂ content in the CIA calculation, the composition of the source rock and the
558 effect of K addition during diagenesis can potentially influence the CIA index.
559 Typically, mafic igneous rocks rich in ferromagnesian content can generate
560 misleading interpretations (Fedo and Babechuk, 2022). In other words, the CIA index
561 must be used to the study of feldspar-hosted rocks of the upper continental crust and
562 derived sediments. The Erguita sedimentary rocks fulfill this criterion as we observe a
563 felsic provenance with related minerals like K-feldspars and quartz (Fig. S1). Our
564 observations indicate that the CIA values are reliable.

565 The upper Erguita sequence of Eocene age (El Bamiki et al., 2020) shows the
566 highest CIA and MS values. The climate state in the Paleogene was highly dynamic
567 with long-term warming (e.g., early Danian) and cooling (e.g., mid-Danian to early
568 Thanetian) periods (Westerhold et al., 2020). In addition, a 9-million-years
569 unprecedented hothouse state occurred during the early Eocene – also known as the
570 Early Eocene Climatic Optimum (EECO), when temperatures were >10°C warmer
571 than today. As a corollary, the rise of atmospheric CO₂ concentrations increases
572 temperature and precipitation, thereby enhancing chemical weathering (Walker et al.,
573 1981; Warr, 2022). In the upper Erguita section, we propose that the EEOC possibly
574 drove up the supply of detrital magnetic components to the shallow waters. Also, our
575 model should imply any relationship between low CIA, MS values, and colder
576 temperatures. This pattern seems to be preserved during the maximum flooding
577 interval at the Selandian-Thanetian transition (Fig. 4) when temperatures were the
578 coolest of the Paleocene (Westerhold et al., 2020). Considering this, our data
579 indicate that the intensity of weathering induced by climate has a significant impact
580 on the long-term evolution of MS. (Fig. 8c). Our work does not rule out the possibility
581 of minor controls exerted by sea level changes on MS trend during high-frequency
582 perturbations, as proposed by Whalen and Day (2010).

583

584 5.3. Implications for paleoenvironmental and paleoclimatic reconstructions at
585 the Cretaceous/Paleogene transition

586 Our combined analyses of rock magnetism, mineralogy, and geochemistry show that
587 MS is an adequate proxy of the long-term evolution of weathering intensity.
588 Understanding the MS evolution has considerable implications for unraveling
589 processes that drove the low MS signal in the decimeter-thick sediments immediately
590 underlying the K-Pg boundary (e.g., Abrajevitch et al., 2015; Font et al., 2011; Lowrie
591 et al., 1990). To explain this low MS interval, unresolved debates suggest a post-
592 depositional dissolution of ferromagnetic minerals (Lowrie et al., 1990) or an increase
593 in atmospheric and oceanic acidity linked to Deccan Traps volcanism (Abrajevitch et
594 al., 2015) to explain this low susceptibility interval. The putative discovery of chloride-
595 rich iron oxyhydroxides (i.e., akaganéite) in stratigraphic horizons of low MS values
596 below the K-Pg boundary from three distinct European sections could confirm the
597 latter view (Font et al., 2017). Primary akaganéite formation requires large
598 concentrations of both dissolved ferrous iron and chloride ions, acidic and oxidizing
599 conditions, and elevated temperatures (Johnston, 1977; Schwertmann and Cornell,
600 1991). Such conditions are typically observed in hydrothermal deposits of the Mid-
601 Atlantic ridge (Bogdanov et al., 2008; Chavagnac et al., 2018). In contrast, the Late
602 Cretaceous akaganéite could have been formed in the acidic and chloride-rich
603 Deccan volcanic plume and subsequently transported several thousands of
604 kilometers away as aerosols (Font et al., 2017). However, linking low MS values to
605 global environmental acidification triggered by Deccan volcanism in stratigraphic
606 horizons containing Cl-rich iron oxyhydroxides may not be straightforward. This is
607 because the akaganéite formation and the mechanism responsible for the MS
608 decrease could have occurred independently.

609 Our study emphasizes that the decrease of magnetic mineral content (i.e.,
610 lower MS values) immediately underlying the K-Pg boundary could now be
611 interpreted differently, although no direct evidence for relationships between MS
612 signal and weathering intensity over a few thousand years has so far been
613 documented. This is further supported by previous assessments of CIA in the
614 Yacoraite and Mingshui formations from northwestern Argentina and northeastern
615 China, respectively (Gao et al., 2021; Rohais et al., 2019). These sediments have
616 recorded a decrease in chemical weathering intensity prior to the K-Pg boundary.
617 Furthermore, oxygen isotopic compositions of the Bidart (France) section correlated

618 with those of the South Atlantic deep-sea site indicate a climate cooling in sediments
619 containing the low MS interval during the last thousands of years of the Maastrichtian
620 (Font et al., 2014; Li and Keller, 1998). Consequently, the weathering intensity could
621 have decreased, leading to reduced delivery of magnetic minerals from land to the
622 oceans. Therefore, it is important to use caution when interpreting MS data with
623 regard to paleoenvironmental changes, such as global environmental acidification.
624 The low weathering intensity and MS values before the K-Pg boundary could provide
625 evidence of a mechanistic link between MS and weathering regime over thousand-
626 year timescales.

627

628 **6. Conclusion**

629 Combined magnetic susceptibility, mineralogical, and geochemical investigations are
630 presented here for the continuous Upper Cretaceous/Paleogene Erguita sedimentary
631 sequence. Moderate chemical weathering would have facilitated the supply of
632 magnetic detritus (both Fe-bearing phyllosilicates and ferromagnetic *sensu lato*
633 minerals) to the oceans (Fig. 8c). These minerals may have been inherited from
634 weathered parent rocks, sediments, or soils of the Anti-Atlas. Our observations hint
635 that the evolution of magnetic susceptibility over millions of years in the Erguita
636 section correlates with weathering intensity as a response to the Paleogene climate
637 change. This work provides evidence for a new weathering proxy. We conclude that
638 the Moroccan Erguita section could offer new insights into the origin of the low
639 susceptibility zone at the K-Pb boundary.

640

641 **Acknowledgements**

642 Thanks to the scientific board of Geoscience Montpellier for supporting this work. The
643 University of Mohammed VI Polytechnic is deeply thanked for field-trip logistics. We
644 are grateful to Bernard Fraisse for his technical assistance during XRD
645 measurements at RRXG platform of University of Montpellier. We would also like to
646 thank Corine Reibel for her technical expertise and the MPMS measurements at
647 IGCM

648 **References**

- 649 Abrajevitch, A., Font, E., Florindo, F., Roberts, A.P., 2015. Asteroid impact vs. Deccan
650 eruptions: The origin of low magnetic susceptibility beds below the Cretaceous–Paleogene
651 boundary revisited. *Earth and Planetary Science Letters* 430, 209–223.
652 <https://doi.org/10.1016/j.epsl.2015.08.022>
- 653 Alibo, D.S., Nozaki, Y., 1999. Rare earth elements in seawater: particle association, shale-
654 normalization, and Ce oxidation. *Geochimica et Cosmochimica Acta* 63, 363–372.
655 [https://doi.org/10.1016/S0016-7037\(98\)00279-8](https://doi.org/10.1016/S0016-7037(98)00279-8)
- 656 Ambroggi, R., 1963. Etude géologique du versant méridional du Haut Atlas occidental et de
657 la plaine du Souss. Université de Paris, Paris.
- 658 Aubineau, J., Parat, F., Chi Fru, E., El Bamiki, R., Mauguin, O., Baron, F., Poujol, M.,
659 Séranne, M., 2022a. Geodynamic seawater-sediment porewater evolution of the east
660 central Atlantic Paleogene ocean margin revealed by U-Pb dating of sedimentary
661 phosphates. *Frontiers in Earth Science* 10:997008.
662 <https://doi.org/10.3389/feart.2022.997008>
- 663 Aubineau, J., Parat, F., Elghali, A., Raji, O., Addou, A., Bonnet, C., Muñoz, M., Mauguin, O.,
664 Baron, F., Jouti, M.B., Yazami, O.K., Bodinier, J.-L., 2022b. Highly variable content of
665 fluorapatite-hosted CO_3^{2-} in the Upper Cretaceous/Paleogene phosphorites (Morocco) and
666 implications for paleodepositional conditions. *Chemical Geology* 597, 120818.
667 <https://doi.org/10.1016/j.chemgeo.2022.120818>
- 668 Aubineau, J., Parat, F., Pierson-Wickmann, A.-C., Séranne, M., Fru, E.C., El Bamiki, R.,
669 Elghali, A., Raji, O., Muñoz, M., Bonnet, C., Jourani, E.-S., Yazami, O.K., Bodinier, J.-L.,
670 2024a. Phosphate $\delta^{13}\text{C}_{\text{org}}$ chemostratigraphy from the Gantour basin, Morocco: A proof
671 of concept from the K–Pg transition to mid-Thanetian. *Chemical Geology* 121861.
672 <https://doi.org/10.1016/j.chemgeo.2023.121861>
- 673 Aubineau, J., Séranne, M., Chi Fru, E., Poujol, M., El Bamiki, R., Antonio, P.Y.J., Muñoz,
674 M., Elghali, A., Raji, O., Jourani, E.-S., Bodinier, J.-L., Parat, F., 2024b. Deciphering the
675 U-Pb dates of sedimentary phosphates: A complex example from the Upper Cretaceous-
676 Lower Paleogene series in northwestern Morocco. *Chemical Geology* 661, 122178.
677 <https://doi.org/10.1016/j.chemgeo.2024.122178>
- 678 Aubourg, C., Robion, P., 2002. Composite ferromagnetic fabrics (magnetite, greigite)
679 measured by AMS and partial AARM in weakly strained sandstones from western
680 Makran, Iran. *Geophysical Journal International* 151, 729–737.
681 <https://doi.org/10.1046/j.1365-246X.2002.01800.x>
- 682 Aubourg, C., Smith, B., Bakhtari, K., Guya, N., Eshragi, A., Lallemand, S., Molinaro, M.,
683 Braud, X., Delaunay, S., 2004. Post-Miocene shortening pictured by magnetic fabric
684 across the Zagros-Makran syntaxis (Iran), in: Sussman, A.J., Weil, A.B. (Eds.), *Orogenic
685 Curvature: Integrating Paleomagnetic and Structural Analyses*. Geological Society of
686 America Special paper, pp. 11–4à.
- 687 Averbuch, O., Tribovillard, N., Devleeschouwer, X., Riquier, L., Mistiaen, B., Van Vliet-
688 Lanoe, B., 2005. Mountain building-enhanced continental weathering and organic carbon
689 burial as major causes for climatic cooling at the Frasnian–Famennian boundary (c. 376
690 Ma)? *Terra Nova* 17, 25–34. <https://doi.org/10.1111/j.1365-3121.2004.00580.x>
- 691 Bau, M., Dulski, P., 1996. Distribution of yttrium and rare-earth elements in the Penge and
692 Kuruman iron-formations, Transvaal Supergroup, South Africa. *Precambrian Research* 79,
693 37–55. [https://doi.org/10.1016/0301-9268\(95\)00087-9](https://doi.org/10.1016/0301-9268(95)00087-9)
- 694 Bau, M., Möller, P., Dulski, P., 1997. Yttrium and lanthanides in eastern Mediterranean
695 seawater and their fractionation during redox-cycling. *Marine Chemistry* 56, 123–131.
696 [https://doi.org/10.1016/S0304-4203\(96\)00091-6](https://doi.org/10.1016/S0304-4203(96)00091-6)
- 697 Bilardello, D., 2021. Late Paleozoic Depositional Environments and Sediment Transport

698 Directions of the Itararé Group Rocks From the State of São Paulo, Brazil, Determined
699 From Rock Magnetism and Magnetic Anisotropy. *Earth and Space Science* 8,
700 e2021EA001703. <https://doi.org/10.1029/2021EA001703>

701 Bilardello, D., Jackson, M., 2013. Cover article: What do the Mumpsies do? *IRM Quarterly*
702 23.

703 Bogdanov, Yu.A., Vikent'ev, I.V., Lein, A.Yu., Bogdanova, O.Yu., Sagalevich, A.M.,
704 Sivtsov, A.V., 2008. Low-temperature hydrothermal deposits in the rift zone of the Mid-
705 Atlantic Ridge. *Geol. Ore Deposits* 50, 119–134.
706 <https://doi.org/10.1134/S1075701508020037>

707 Borradaile, G.J., Puumala, M.A., 1989. Synthetic magnetic fabrics in a plasticene medium.
708 *Tectonophysics* 164, 73–78. [https://doi.org/10.1016/0040-1951\(89\)90235-7](https://doi.org/10.1016/0040-1951(89)90235-7)

709 Boulila, S., de Rafélis, M., Hinnov, L.A., Gardin, S., Galbrun, B., Collin, P.-Y., 2010.
710 Orbitally forced climate and sea-level changes in the Paleoeceanic Tethyan domain (marl–
711 limestone alternations, Lower Kimmeridgian, SE France). *Palaeogeography,*
712 *Palaeoclimatology, Palaeoecology* 292, 57–70.
713 <https://doi.org/10.1016/j.palaeo.2010.03.026>

714 Boulila, S., Galbrun, B., Hinnov, L.A., Collin, P.-Y., 2008. Orbital calibration of the Early
715 Kimmeridgian (southeastern France): implications for geochronology and sequence
716 stratigraphy. *Terra Nova* 20, 455–462. <https://doi.org/10.1111/j.1365-3121.2008.00838.x>

717 Brindley, G.W., Brown, G., 1980. Crystal structure of clay minerals and their X-ray
718 identification. Mineralogical Society, London.

719 Burchette, T.P., Wright, V.P., 1992. Carbonate ramp depositional systems. *Sedimentary*
720 *Geology* 79, 3–57. [https://doi.org/10.1016/0037-0738\(92\)90003-A](https://doi.org/10.1016/0037-0738(92)90003-A)

721 Carignan, J., Hild, P., Mevelle, G., Morel, J., Yeghicheyan, D., 2001. Routine analyses of
722 trace elements in geological samples using flow injection and low pressure on-line liquid
723 chromatography coupled to ICP-MS: a study of geochemical reference materials BR, DR-
724 N, UB-N, AN-G and GH. *Geostandards Newsletter* 25, 187–198.
725 <https://doi.org/10.1111/j.1751-908X.2001.tb00595.x>

726 Chadima, M., Jelínek, V., 2008. Anisoft 4.2. – Anisotropy data browser. *Paleo, Rock and*
727 *Environmental Magnetism, 11th Castle Meeting. Contributions to Geophysics & Geodesy,*
728 *Special Issue.*

729 Charton, R., Bertotti, G., Arnould, A.D., Storms, J.E.A., Redfern, J., 2021. Low- temperature
730 thermochronology as a control on vertical movements for semi- quantitative
731 source- to- sink analysis: A case study for the Permian to Neogene of Morocco and
732 surroundings. *Basin Research* 33, 1337–1383. <https://doi.org/10.1111/bre.12517>

733 Chavagnac, V., Leleu, T., Fontaine, F., Cannat, M., Ceuleneer, G., Castillo, A., 2018. Spatial
734 Variations in Vent Chemistry at the Lucky Strike Hydrothermal Field, Mid-Atlantic Ridge
735 (37°N): Updates for Subseafloor Flow Geometry From the Newly Discovered Capelinhos
736 Vent. *Geochemistry, Geophysics, Geosystems* 19, 4444–4458.
737 <https://doi.org/10.1029/2018GC007765>

738 Clarkson, M.O., Poulton, S.W., Guilbaud, R., Wood, R.A., 2014. Assessing the utility of
739 Fe/Al and Fe-speciation to record water column redox conditions in carbonate-rich
740 sediments. *Chemical Geology* 382, 111–122.
741 <https://doi.org/10.1016/j.chemgeo.2014.05.031>

742 Cosmidis, J., Benzerara, K., Gheerbrant, E., Estève, I., Bouya, B., Amaghazaz, M., 2013.
743 Nanometer-scale characterization of exceptionally preserved bacterial fossils in Paleocene
744 phosphorites from Ouled Abdoun (Morocco). *Geobiology* 11, 139–153.
745 <https://doi.org/10.1111/gbi.12022>

746 Crick, R.E., Ellwood, B.B., Hassani, A.E., Feist, R., Hladil, J., 1997. MagnetoSusceptibility
747 Event and Cyclostratigraphy (MSEC) of the Eifelian-Givetian GSSP and associated

748 boundary sequences in north Africa and Europe. *Episodes Journal of International*
749 *Geoscience* 20, 167–175. <https://doi.org/10.18814/epiugs/1997/v20i3/004>

750 Da Silva, A.C., De Vleeschouwer, D., Boulvain, F., Claeys, P., Fagel, N., Humblet, M.,
751 Mabilille, C., Michel, J., Sardar Abadi, M., Pas, D., Dekkers, M.J., 2013. Magnetic
752 susceptibility as a high-resolution correlation tool and as a climatic proxy in Paleozoic
753 rocks – Merits and pitfalls: Examples from the Devonian in Belgium. *Marine and*
754 *Petroleum Geology* 46, 173–189. <https://doi.org/10.1016/j.marpetgeo.2013.06.012>

755 Da Silva, A.-C., Mabilille, C., Boulvain, F., 2009. Influence of sedimentary setting on the use
756 of magnetic susceptibility: examples from the Devonian of Belgium. *Sedimentology* 56,
757 1292–1306. <https://doi.org/10.1111/j.1365-3091.2008.01034.x>

758 Da Silva, A.-C., Sinnesael, M., Claeys, P., Davies, J.H.F.L., de Winter, N.J., Percival, L.M.E.,
759 Schaltegger, U., De Vleeschouwer, D., 2020. Anchoring the Late Devonian mass
760 extinction in absolute time by integrating climatic controls and radio-isotopic dating. *Sci*
761 *Rep* 10, 12940. <https://doi.org/10.1038/s41598-020-69097-6>

762 Da Silva, A.C., Whalen, M.T., Hladil, J., Chadimova, L., Chen, D., Spassov, S., Boulvain, F.,
763 Devleeschouwer, X., 2015. Magnetic susceptibility application: a window onto ancient
764 environments and climatic variations: foreword. *Geological Society, London, Special*
765 *Publications* 414, 1–13. <https://doi.org/10.1144/SP414.12>

766 Da Silva, A.-C., Yans, J., Boulvain, F., 2010. *Sedimentology and magnetic susceptibility*
767 *during the “punctata” event of the Ardenne area (Belgium): identification of severe and*
768 *rapid sea level fluctuations*, in: Da Silva, A.-C., Boulvain, F. (Eds.), *Magnetic*
769 *Susceptibility, Correlations and Palaeozoic Environments*. pp. 319–322.

770 De Baar, H.J.W., Brewer, P.G., Bacon, M.P., 1985. Anomalies in rare earth distributions in
771 seawater: Gd and Tb. *Geochimica et Cosmochimica Acta* 49, 1961–1969.
772 [https://doi.org/10.1016/0016-7037\(85\)90090-0](https://doi.org/10.1016/0016-7037(85)90090-0)

773 Dekkers, M.J., 1989. Magnetic Properties of Natural Goethite—II. TRM Behaviour During
774 Thermal and Alternating Field Demagnetization and Low-Temperature Treatment.
775 *Geophysical Journal International* 97, 341–355. <https://doi.org/10.1111/j.1365-246X.1989.tb00505.x>

776
777 Döbelin, N., Kleeberg, R., 2015. Profex: a graphical user interface for the Rietveld
778 refinement program BGMN. *J Appl Cryst* 48, 1573–1580.
779 <https://doi.org/10.1107/S1600576715014685>

780 Dunlop, D.J., Özdemir, Ö. (Eds.), 1997. *Rock Magnetism: Fundamentals and Frontiers*.
781 *Cambridge Studies in Magnetism*.

782 El Bamiki, R., Raji, O., Ouabid, M., Elghali, A., Khadiri Yazami, O., Bodinier, J.-L., 2021.
783 *Phosphate Rocks: A Review of Sedimentary and Igneous Occurrences in Morocco*.
784 *Minerals* 11, 1137. <https://doi.org/10.3390/min11101137>

785 El Bamiki, R., Séranne, M., Chellaï, E.H., Merzeraud, G., Marzoqi, M., Melinte-Dobrinescu,
786 M.C., 2020. The Moroccan High Atlas phosphate-rich sediments: Unraveling the
787 accumulation and differentiation processes. *Sedimentary Geology* 403, 105655.
788 <https://doi.org/10.1016/j.sedgeo.2020.105655>

789 El Bamiki, R., Séranne, M., Parat, F., Aubineau, J., Chellaï, E.H., Marzoqi, M., Bodinier, J.-
790 L., 2023. Post-phosphogenesis processes and the natural beneficiation of phosphates:
791 Geochemical evidence from the Moroccan High Atlas phosphate-rich sediments. *Chemical*
792 *Geology* 631, 121523. <https://doi.org/10.1016/j.chemgeo.2023.121523>

793 Ellouz, N., Patriat, M., Gaulier, J.-M., Bouatmani, R., Sabounji, S., 2003. From rifting to
794 Alpine inversion: Mesozoic and Cenozoic subsidence history of some Moroccan basins.
795 *Sedimentary Geology* 156, 185–212. [https://doi.org/10.1016/S0037-0738\(02\)00288-9](https://doi.org/10.1016/S0037-0738(02)00288-9)

796 Ellwood, B.B., Crick, R.E., El Hassani, A., 1999. The Magneto-Susceptibility Event and
797 Cyclostratigraphy (MSEC) Method Used in Geological Correlation of Devonian Rocks

798 from Anti-Atlas Morocco1. AAPG Bulletin 83, 1119–1134.
799 <https://doi.org/10.1306/E4FD2E8D-1732-11D7-8645000102C1865D>

800 Ellwood, B.B., Crick, R.E., Hassani, A.E., Benoist, S.L., Young, R.H., 2000.
801 Magnetosusceptibility event and cyclostratigraphy method applied to marine rocks:
802 Detrital input versus carbonate productivity. *Geology* 28, 1135–1138.
803 [https://doi.org/10.1130/0091-7613\(2000\)28<1135:MEACMA>2.0.CO;2](https://doi.org/10.1130/0091-7613(2000)28<1135:MEACMA>2.0.CO;2)

804 Ellwood, B.B., El Hassani, A., Tomkins, J.H., Bultynck, P., 2015. A climate-driven model
805 and development of a floating-point timescale for the middle devonian Eifelian stage using
806 time-series analysis of magnetic susceptibility (x) data set, in: Da Silva, A.C., Whalen,
807 M.T., Hladil, J., Chadimova, L., Chen, D., Spassov, S., Boulvain, F., Devleeschouwer, X.
808 (Eds.), *Magnetic Susceptibility Application – a Window onto Ancient Environments and*
809 *Climatic Variations*.

810 Fedo, C.M., Babechuk, M.G., 2022. Petrogenesis of siliciclastic sediments and sedimentary
811 rocks explored in three-dimensional Al₂O₃–CaO*+Na₂O–K₂O–FeO+MgO (A–CN–K–
812 FM) compositional space. *Canadian Journal of Earth Sciences* 60, 818–838.
813 <https://doi.org/10.1139/cjes-2022-0051>

814 Fedo, C.M., Wayne Nesbitt, H., Young, G.M., 1995. Unraveling the effects of potassium
815 metasomatism in sedimentary rocks and paleosols, with implications for paleoweathering
816 conditions and provenance. *Geology* 23, 921–924. [https://doi.org/10.1130/0091-7613\(1995\)023<0921:UTEOPM>2.3.CO;2](https://doi.org/10.1130/0091-7613(1995)023<0921:UTEOPM>2.3.CO;2)

818 Flinn, D., 1978. Construction and computation of three-dimensional progressive
819 deformations. *Journal of the Geological Society* 135, 291–305.
820 <https://doi.org/10.1144/gsjgs.135.3.0291>

821 Font, E., Carlut, J., Rémazeilles, C., Mather, T.A., Nédélec, A., Mirão, J., Casale, S., 2017.
822 End-Cretaceous akaganéite as a mineral marker of Deccan volcanism in the sedimentary
823 record. *Sci Rep* 7, 11453. <https://doi.org/10.1038/s41598-017-11954-y>

824 Font, E., Fabre, S., Nédélec, A., Adatte, T., Keller, G., Viega-Pires, C., Ponte, J., Mirão, J.,
825 Khozyem, H., Spangenberg, J.E., 2014. Atmospheric halogen and acid rains during the
826 main phase of Deccan eruptions: Magnetic and mineral evidence, in: Keller, G., Kerr, A.C.
827 (Eds.), *Volcanism, Impacts, and Mass Extinctions: Causes and Effects*. Geological Society
828 of America, pp. 353–368.

829 Font, E., Nédélec, A., Ellwood, B.B., Mirão, J., Silva, P.F., 2011. A new sedimentary
830 benchmark for the Deccan Traps volcanism? *Geophysical Research Letters* 38.
831 <https://doi.org/10.1029/2011GL049824>

832 Frizon de Lamotte, D., Zizi, M., Missenard, Y., Hafid, M., El Azzouzi, M., Maury, R.C.,
833 Charrière, A., Taki, Z., Benammi, M., Michard, A., 2008. The Atlas System, in: Michard,
834 André, Saddiqi, O., Chalouan, A., Frizon de Lamotte, Dominique (Eds.), *Continental*
835 *Evolution: The Geology of Morocco: Structure, Stratigraphy, and Tectonics of the Africa-*
836 *Atlantic-Mediterranean Triple Junction*, Lecture Notes in Earth Sciences. Springer, Berlin,
837 Heidelberg, pp. 133–202. https://doi.org/10.1007/978-3-540-77076-3_4

838 Frizon de Lamotte, D.F., Leturmy, P., Missenard, Y., Khomsi, S., Ruiz, G., Saddiqi, O.,
839 Guillocheau, F., Michard, A., 2009. Mesozoic and Cenozoic vertical movements in the
840 Atlas system (Algeria, Morocco, Tunisia): An overview. *Tectonophysics* 475, 9–28.
841 <https://doi.org/10.1016/j.tecto.2008.10.024>

842 Gao, Yuan, Ibarra, D.E., Caves Rugenstein, J.K., Chen, J., Kukla, T., Methner, K., Gao,
843 Youfeng, Huang, H., Lin, Z., Zhang, L., Xi, D., Wu, H., Carroll, A.R., Graham, S.A.,
844 Chamberlain, C.P., Wang, C., 2021. Terrestrial climate in mid-latitude East Asia from the
845 latest Cretaceous to the earliest Paleogene: A multiproxy record from the Songliao Basin in
846 northeastern China. *Earth-Science Reviews* 216, 103572.
847 <https://doi.org/10.1016/j.earscirev.2021.103572>

848 Garnit, H., Bouhlel, S., Barca, D., Chtara, C., 2012. Application of LA-ICP-MS to
849 sedimentary phosphatic particles from Tunisian phosphorite deposits: Insights from trace
850 elements and REE into paleo-depositional environments. *Geochemistry* 72, 127–139.
851 <https://doi.org/10.1016/j.chemer.2012.02.001>

852 Girard, C., Feist, R., Mossoni, A., Cornée, J.-J., Camps, P., Charruault, A.-L., Corradini, C.,
853 2021. North-Gondwana – Laurussia dynamic paleogeography challenged by magnetic
854 susceptibility through the Famennian. *Gondwana Research* 97, 263–272.
855 <https://doi.org/10.1016/j.gr.2021.06.002>

856 Herbig, H.-G., Trappe, J., 1994. Stratigraphy of the Subatlas Group (Maastrichtian - Middle
857 Eocene, Morocco). *Newsletters on Stratigraphy* 125–165.
858 <https://doi.org/10.1127/nos/30/1994/125>

859 Hillier, S., 2000. Accurate quantitative analysis of clay and other minerals in sandstones by
860 XRD: comparison of a Rietveld and a reference intensity ratio (RIR) method and the
861 importance of sample preparation. *Clay Minerals* 35, 291–302.
862 <https://doi.org/10.1180/000985500546666>

863 Hladil, J., 2002. Geophysical records of dispersed weathering products on the Frasnian
864 carbonate platform and early Famennian ramps in Moravia, Czech Republic: proxies for
865 eustasy and palaeoclimate. *Palaeogeography, Palaeoclimatology, Palaeoecology* 181, 213–
866 250. [https://doi.org/10.1016/S0031-0182\(01\)00480-1](https://doi.org/10.1016/S0031-0182(01)00480-1)

867 Jelinek, V., 1981. Characterization of the magnetic fabric of rocks. *Tectonophysics* 79, T63–
868 T67. [https://doi.org/10.1016/0040-1951\(81\)90110-4](https://doi.org/10.1016/0040-1951(81)90110-4)

869 Jian, X., Guan, P., Zhang, W., Feng, F., 2013. Geochemistry of Mesozoic and Cenozoic
870 sediments in the northern Qaidam basin, northeastern Tibetan Plateau: Implications for
871 provenance and weathering. *Chemical Geology* 360–361, 74–88.
872 <https://doi.org/10.1016/j.chemgeo.2013.10.011>

873 Johnston, J.H., 1977. Jarosite and akaganéite from White Island volcano, New Zealand: an X-
874 ray and Mössbauer study. *Geochimica et Cosmochimica Acta* 41, 539–544.

875 Knidiri, A., Daoudi, L., El Ouahabi, M., Rhouta, B., Rocha, F., Fagel, N., 2014.
876 Palaeogeographic controls on palygorskite occurrence in Maastrichtian-Palaeogene
877 sediments of the Western High Atlas and Meseta Basins (Morocco). *Clay Minerals* 49,
878 595–608. <https://doi.org/10.1180/claymin.2014.049.4.08>

879 Kocsis, L., Gheerbrant, E., Mouflih, M., Cappetta, H., Yans, J., Amaghazaz, M., 2014.
880 Comprehensive stable isotope investigation of marine biogenic apatite from the late
881 Cretaceous–early Eocene phosphate series of Morocco. *Palaeogeography,
882 Palaeoclimatology, Palaeoecology* 394, 74–88.
883 <https://doi.org/10.1016/j.palaeo.2013.11.002>

884 Kostrov, A., 2002. Low-temperature magnetic hysteresis properties of partially oxidized
885 magnetite. *Geophysical Journal International* 149, 796–804. <https://doi.org/10.1046/j.1365-246X.2002.01686.x>

887 Lanari, R., Fellin, M.G., Faccenna, C., Balestrieri, M.L., Pazzaglia, F.J., Youbi, N., Maden,
888 C., 2020. Exhumation and Surface Evolution of the Western High Atlas and Surrounding
889 Regions as Constrained by Low-Temperature Thermochronology. *Tectonics* 39,
890 e2019TC005562. <https://doi.org/10.1029/2019TC005562>

891 Leprêtre, R., Missenard, Y., Barbarand, J., Gautheron, C., Juvie, I., Saddiqi, O., 2018.
892 Polyphased Inversions of an Intracontinental Rift: Case Study of the Marrakech High
893 Atlas, Morocco. *Tectonics* 37, 818–841. <https://doi.org/10.1002/2017TC004693>

894 Li, L., Keller, G., 1998. Maastrichtian climate, productivity and faunal turnovers in planktic
895 foraminifera in South Atlantic DSDP sites 525A and 21. *Marine Micropaleontology* 33,
896 55–86. [https://doi.org/10.1016/S0377-8398\(97\)00027-3](https://doi.org/10.1016/S0377-8398(97)00027-3)

897 Lowrie, W., Alvarez, W., Asaro, F., 1990. The origin of the White Beds below the

898 Cretaceous-Tertiary boundary in the Gubbio section, Italy. *Earth and Planetary Science*
899 *Letters* 98, 303–312. [https://doi.org/10.1016/0012-821X\(90\)90032-S](https://doi.org/10.1016/0012-821X(90)90032-S)

900 Mahboubi, A., Cornée, J.-J., Feist, R., Camps, P., Girard, C., 2019. Frasnian (Upper
901 Devonian) integrated facies analysis, magnetic susceptibility and sea-level fluctuations in
902 the NW Algerian Sahara. *Geological Magazine* 156, 1295–1310.
903 <https://doi.org/10.1017/S0016756818000626>

904 McClellan, G.H., Van Kauwenbergh, S.J., 1991. Mineralogical and chemical variation of
905 francolites with geological time. *Journal of the Geological Society* 148, 809–812.
906 <https://doi.org/10.1144/gsjgs.148.5.0809>

907 Mead, G.A., Tauxe, L., LaBrecque, J.L., 1986. Oligocene paleoceanography of the South
908 Atlantic: Paleoclimatic implications of sediment accumulation rates and magnetic
909 susceptibility measurements. *Paleoceanography* 1, 273–284.
910 <https://doi.org/10.1029/PA001i003p00273>

911 Meunier, A., Caner, L., Hubert, F., Albani, A.E., Prêt, D., 2013. The weathering intensity
912 scale (WIS): An alternative approach of the Chemical Index of Alteration (CIA). *American*
913 *Journal of Science* 313, 113–143. <https://doi.org/10.2475/02.2013.03>

914 Michard, A., Saddiqi, O., Chalouan, A., Frizon de Lamotte, D., 2008. *Continental Evolution:
915 The Geology of Morocco*. Springer, Berlin, Heidelberg.

916 Missenard, Y., Saddiqi, O., Barbarand, J., Leturmy, P., Ruiz, G., El Haimer, F.-Z., Frizon de
917 Lamotte, D., 2008. Cenozoic denudation in the Marrakech High Atlas, Morocco: insight
918 from apatite fission-track thermochronology. *Terra Nova* 20, 221–228.
919 <https://doi.org/10.1111/j.1365-3121.2008.00810.x>

920 Morin, F.J., 1950. Magnetic Susceptibility of $\alpha\text{-Fe}_2\text{O}_3$ and $\alpha\text{-Fe}_2\text{O}_3$ with Added
921 Titanium. *Phys. Rev.* 78, 819–820. <https://doi.org/10.1103/PhysRev.78.819.2>

922 Nathan, Y., 1984. The Mineralogy and Geochemistry of Phosphorites, in: Nriagu, J.O.,
923 Moore, P.B. (Eds.), *Phosphate Minerals*. Springer-Verlag, Berlin, Heidelberg, pp. 275–
924 291.

925 Nesbitt, H.W., Young, G.M., 1982. Early Proterozoic climates and plate motions inferred
926 from major element chemistry of lutites. *Nature* 299, 715–717.
927 <https://doi.org/10.1038/299715a0>

928 Nguidi, M.A., Mouflih, M., Benbouziane, A., Kocsis, L., El Ouariti, S., El Boukhari, H.,
929 Aquit, M., Yazami, O.K., 2021. Lithofacies analysis, sedimentary dynamics and genesis of
930 Maastrichtian-Eocene phosphorites of BouCraa deposit (Southern Morocco). *Journal of*
931 *African Earth Sciences* 177, 104161. <https://doi.org/10.1016/j.jafrearsci.2021.104161>

932 Nowaczyk, N.R., Minyuk, P., Melles, M., Brigham-Grette, J., Glushkova, O., Nolan, M.,
933 Lozhkin, A.V., Stetsenko, T.V., M. Andersen, P., Forman, S.L., 2002.
934 Magnetostratigraphic results from impact crater Lake El'gygytgyn, northeastern Siberia: a
935 300 kyr long high-resolution terrestrial palaeoclimatic record from the Arctic. *Geophysical*
936 *Journal International* 150, 109–126. <https://doi.org/10.1046/j.1365-246X.2002.01625.x>

937 Özdemir, Ö., Dunlop, D.J., 2010. Hallmarks of maghemitization in low-temperature
938 remanence cycling of partially oxidized magnetite nanoparticles. *Journal of Geophysical*
939 *Research: Solid Earth* 115. <https://doi.org/10.1029/2009JB006756>

940 Özdemir, Ö., Dunlop, D.J., 2005. Thermoremanent magnetization of multidomain hematite.
941 *Journal of Geophysical Research: Solid Earth* 110. <https://doi.org/10.1029/2005JB003820>

942 Özdemir, Ö., Dunlop, D.J., Moskowitz, B.M., 2002. Changes in remanence, coercivity and
943 domain state at low temperature in magnetite. *Earth and Planetary Science Letters* 194,
944 343–358. [https://doi.org/10.1016/S0012-821X\(01\)00562-3](https://doi.org/10.1016/S0012-821X(01)00562-3)

945 Pas, D., Da Silva, A.-C., Poulain, G., Spassov, S., Boulvain, F., 2019. Magnetic Susceptibility
946 Record in Paleozoic Succession (Rhenohercynian Massif, Northern Europe) –
947 Disentangling Sea Level, Local and Diagenetic Impact on the Magnetic Records. *Frontiers*

948 in Earth Science 7.

949 Paterson, G.A., Zhao, X., Jackson, M., Heslop, D., 2018. Measuring, Processing, and
950 Analyzing Hysteresis Data. *Geochem Geophys Geosyst* 19, 1925–1945.
951 <https://doi.org/10.1029/2018GC007620>

952 Potter, D.K., Stephenson, A., 1988. Single-domain particles in rocks and magnetic fabric
953 analysis. *Geophysical Research Letters* 15, 1097–1100.
954 <https://doi.org/10.1029/GL015i010p01097>

955 Pufahl, P.K., Groat, L.A., 2017. Sedimentary and Igneous Phosphate Deposits: Formation and
956 Exploration: An Invited Paper. *Economic Geology* 112, 483–516.
957 <https://doi.org/10.2113/econgeo.112.3.483>

958 Reynard, B., Lécuyer, C., Grandjean, P., 1999. Crystal-chemical controls on rare-earth
959 element concentrations in fossil biogenic apatites and implications for paleoenvironmental
960 reconstructions. *Chemical Geology* 155, 233–241. [https://doi.org/10.1016/S0009-2541\(98\)00169-7](https://doi.org/10.1016/S0009-2541(98)00169-7)

962 Riquier, L., Averbuch, O., Devleeschouwer, X., Tribouvillard, N., 2010. Diagenetic versus
963 detrital origin of the magnetic susceptibility variations in some carbonate Frasnian–
964 Famennian boundary sections from Northern Africa and Western Europe: implications for
965 paleoenvironmental reconstructions. *Int J Earth Sci (Geol Rundsch)* 99, 57–73.
966 <https://doi.org/10.1007/s00531-009-0492-7>

967 Robinson, S.G., 1986. The late Pleistocene palaeoclimatic record of North Atlantic deep-sea
968 sediments revealed by mineral-magnetic measurements. *Physics of the Earth and Planetary
969 Interiors, Physics of the earth and planetary interiors* 42, 22–47.
970 [https://doi.org/10.1016/S0031-9201\(86\)80006-1](https://doi.org/10.1016/S0031-9201(86)80006-1)

971 Rohais, S., Hamon, Y., Deschamps, R., Beaumont, V., Gasparini, M., Pillot, D., Romero-
972 Sarmiento, M.-F., 2019. Patterns of organic carbon enrichment in a lacustrine system
973 across the K-T boundary: Insight from a multi-proxy analysis of the Yacoraite Formation,
974 Salta rift basin, Argentina. *International Journal of Coal Geology* 210, 103208.
975 <https://doi.org/10.1016/j.coal.2019.05.015>

976 Schneider, J., Bechstädt, T., Machel, H.G., 2004. Covariance of C- and O-isotopes with
977 magnetic susceptibility as a result of burial diagenesis of sandstones and carbonates: an
978 example from the Lower Devonian La Vid Group, Cantabrian Zone, NW Spain. *Int J Earth
979 Sci (Geol Rundsch)* 93, 990–1007. <https://doi.org/10.1007/s00531-004-0434-3>

980 Schuffert, J.D., Kastner, M., Emanuele, G., Jahnke, R.A., 1990. Carbonate-ion substitution in
981 francolite: A new equation. *Geochimica et Cosmochimica Acta* 54, 2323–2328.
982 [https://doi.org/10.1016/0016-7037\(90\)90058-S](https://doi.org/10.1016/0016-7037(90)90058-S)

983 Schwertmann, U., Cornell, R.M., 1991. *Iron Oxides in the Laboratory: Preparation and
984 Characterization*. John Wiley & Sons.

985 Shields, G., Stille, P., 2001. Diagenetic constraints on the use of cerium anomalies as
986 palaeoseawater redox proxies: an isotopic and REE study of Cambrian phosphorites.
987 *Chemical Geology, Response of the Oceanic / Atmospheric Systems to Past Global
988 Changes* 175, 29–48. [https://doi.org/10.1016/S0009-2541\(00\)00362-4](https://doi.org/10.1016/S0009-2541(00)00362-4)

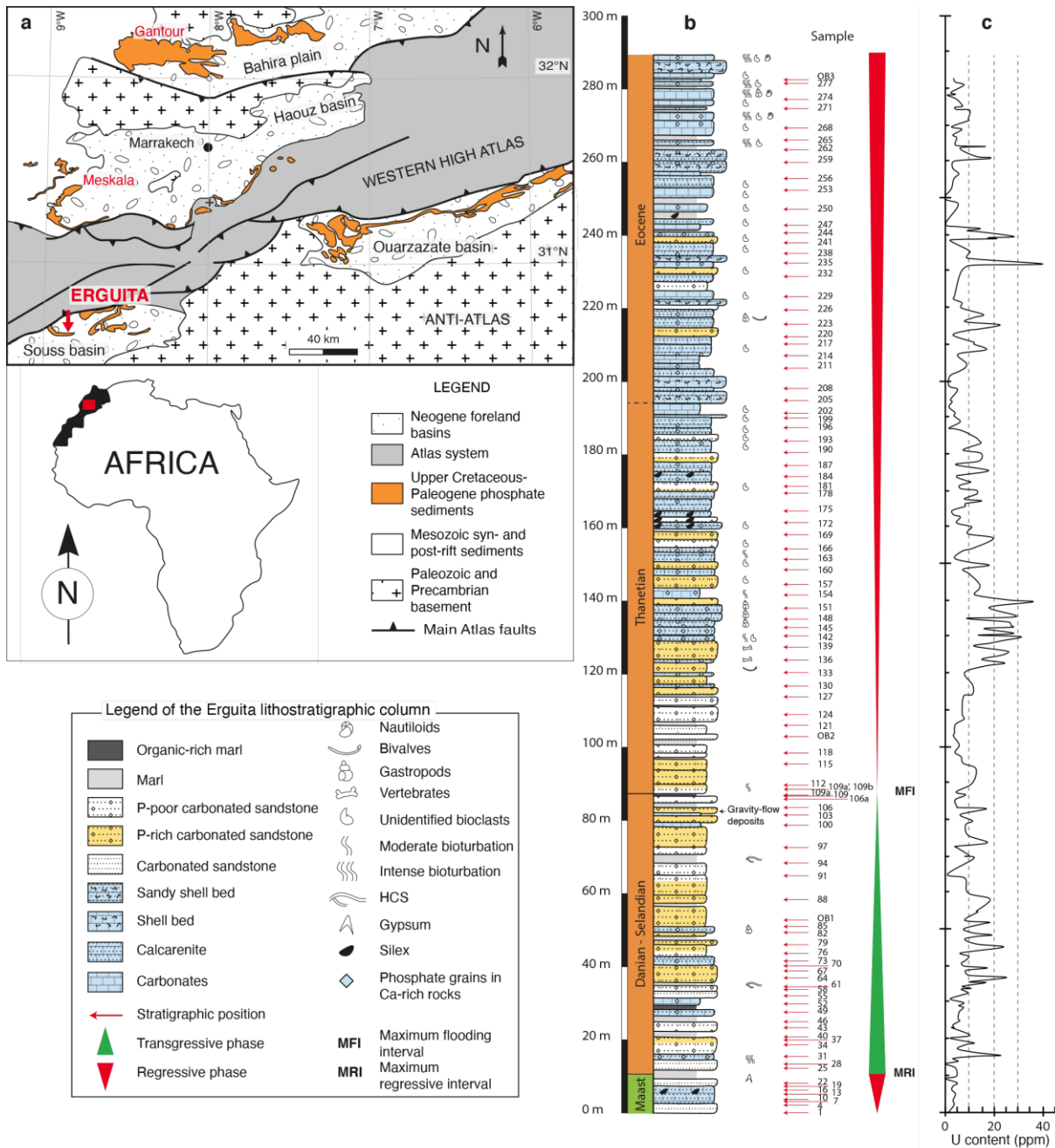
989 Singer, A., Galan, E., 1984. *Palygorskite-Sepiolite: Occurrences, Genesis and Uses*. Elsevier,
990 Amsterdam.

991 Środoń, J., Eberl, D.D., 1984. Illite, in: Bailey, S.W. (Ed.), *Review in Mineralogy Vol. 13,*
992 *Micas*. Mineralogical Society of America, Washington DC, pp. 495–544.

993 Stage, M., 2001. Magnetic susceptibility as carrier of a climatic signal in chalk. *Earth and
994 Planetary Science Letters* 188, 17–27. [https://doi.org/10.1016/S0012-821X\(01\)00304-1](https://doi.org/10.1016/S0012-821X(01)00304-1)

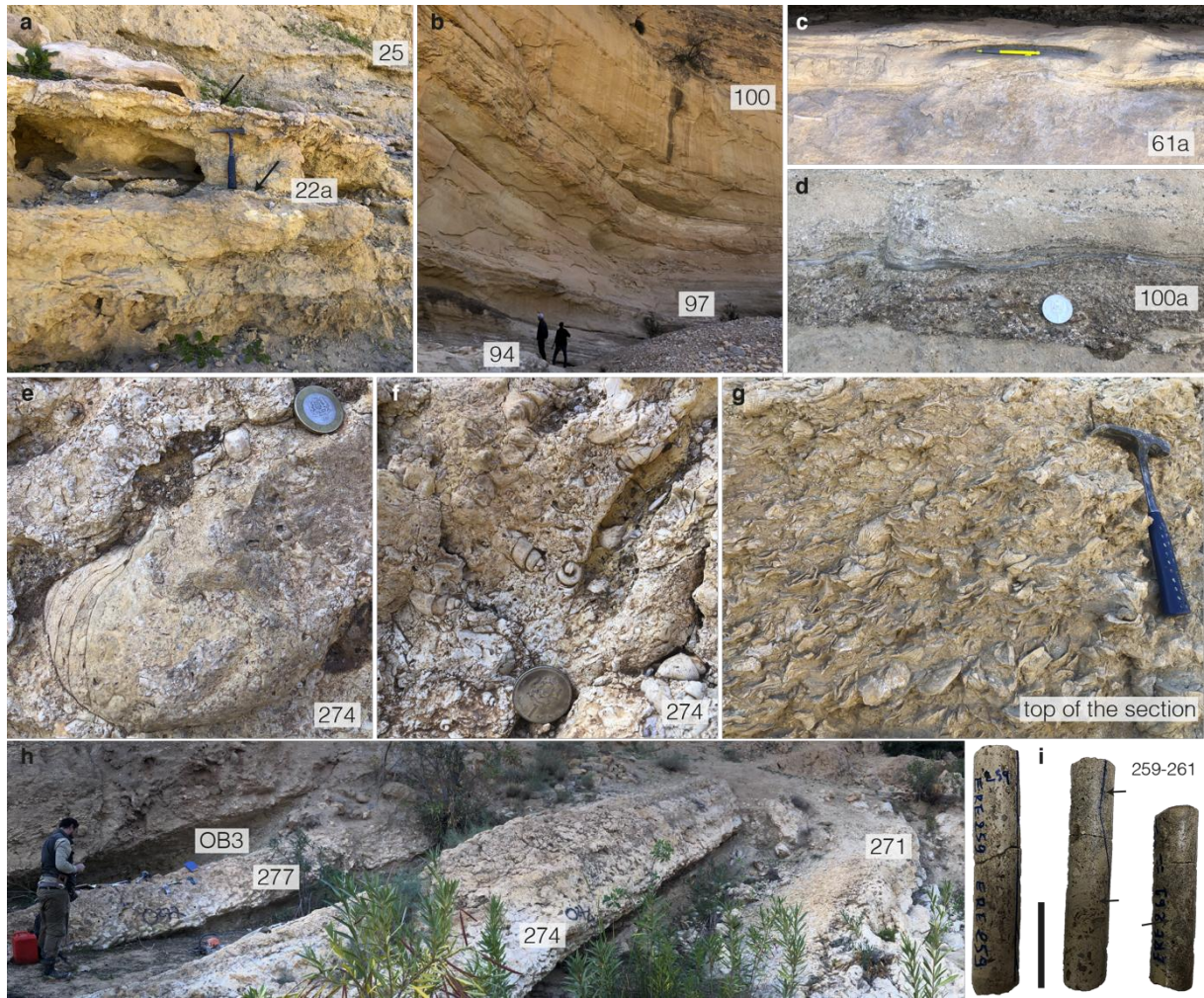
995 Tauxe, L., Gee, J.S., Staudigel, H., 1998. Flow directions in dikes from anisotropy of
996 magnetic susceptibility data: The bootstrap way. *J. Geophys. Res.* 103, 17775–17790.
997 <https://doi.org/10.1029/98JB01077>

- 998 Taylor, S.N., Lagroix, F., Rousseau, D.-D., Antoine, P., 2014. Mineral magnetic
999 characterization of the Upper Pleniglacial Nussloch loess sequence (Germany): an insight
1000 into local environmental processes. *Geophysical Journal International* 199, 1463–1480.
1001 <https://doi.org/10.1093/gji/ggu331>
- 1002 Taylor, S.R., McLennan, S.M., 1985. *The continental crust: Its composition and evolution.*
1003 Blackwell Scientific Publications, Oxford.
- 1004 Vanderaveroot, P., Averbuch, O., Deconinck, J.-F., Chamley, H., 1999. A record of
1005 glacial/interglacial alternations in Pleistocene sediments off New Jersey expressed by clay
1006 mineral, grain-size and magnetic susceptibility data. *Marine Geology* 159, 79–92.
1007 [https://doi.org/10.1016/S0025-3227\(98\)00203-5](https://doi.org/10.1016/S0025-3227(98)00203-5)
- 1008 Velde, B., Suzuki, T., Nicot, E., 1986. Pressure-temperature-composition of illite/smectite
1009 mixed-layer minerals: Niger delta mudstones and other examples. *Clays and Clay Minerals*
1010 34, 435–441.
- 1011 Verwey, E., 1935. The crystal structure of γ -Fe₂O₃ and γ -Al₂O₃. *Zeitschrift für*
1012 *Kristallographie-Crystalline Materials* 91, 65–69.
- 1013 Walker, J.C.G., Hays, P.B., Kasting, J.F., 1981. A negative feedback mechanism for the long-
1014 term stabilization of Earth's surface temperature. *Journal of Geophysical Research: Oceans*
1015 86, 9776–9782. <https://doi.org/10.1029/JC086iC10p09776>
- 1016 Walker, R.G., James, N.P., 1992. *Facies Models: Response to Sea Level Change.* Geological
1017 Association of Canada, Geotext. ed.
- 1018 Warr, L.N., 2022. Earth's clay mineral inventory and its climate interaction: A quantitative
1019 assessment. *Earth-Science Reviews* 234, 104198.
1020 <https://doi.org/10.1016/j.earscirev.2022.104198>
- 1021 Westerhold, T., Marwan, N., Drury, A.J., Liebrand, D., Agnini, C., Anagnostou, E., Barnet,
1022 J.S.K., Bohaty, S.M., De Vleeschouwer, D., Florindo, F., Frederichs, T., Hodell, D.A.,
1023 Holbourn, A.E., Kroon, D., Lauretano, V., Littler, K., Lourens, L.J., Lyle, M., Pälike, H.,
1024 Röhl, U., Tian, J., Wilkens, R.H., Wilson, P.A., Zachos, J.C., 2020. An astronomically
1025 dated record of Earth's climate and its predictability over the last 66 million years. *Science*
1026 369, 1383–1387. <https://doi.org/10.1126/science.aba6853>
- 1027 Whalen, M.T., Day, J.E. (Jed), 2010. Cross-Basin Variations in Magnetic Susceptibility
1028 Influenced by Changing Sea Level, Paleogeography, and Paleoclimate: Upper Devonian,
1029 Western Canada Sedimentary Basin. *Journal of Sedimentary Research* 80, 1109–1127.
1030 <https://doi.org/10.2110/jsr.2010.093>
- 1031 Wouters, S., Spassov, S., Martinez, M., Steurbaut, E., Storme, J.-Y., Yans, J.,
1032 Devleeschouwer, X., 2019. Depositional changes during the Danian–Selandian transition
1033 in Loubieng (France), Zumaia (Spain) and Sidi Nasseur (Tunisia): insights from and limits
1034 of rock magnetism. *Geological Magazine* 156, 1982–2000.
1035 <https://doi.org/10.1017/S0016756819000281>
- 1036 Zhang, R., Kravchinsky, V.A., Zhu, R., Yue, L., 2010. Paleomonsoon route reconstruction
1037 along a W–E transect in the Chinese Loess Plateau using the anisotropy of magnetic
1038 susceptibility: Summer monsoon model. *Earth and Planetary Science Letters* 299, 436–
1039 446. <https://doi.org/10.1016/j.epsl.2010.09.026>
- 1040

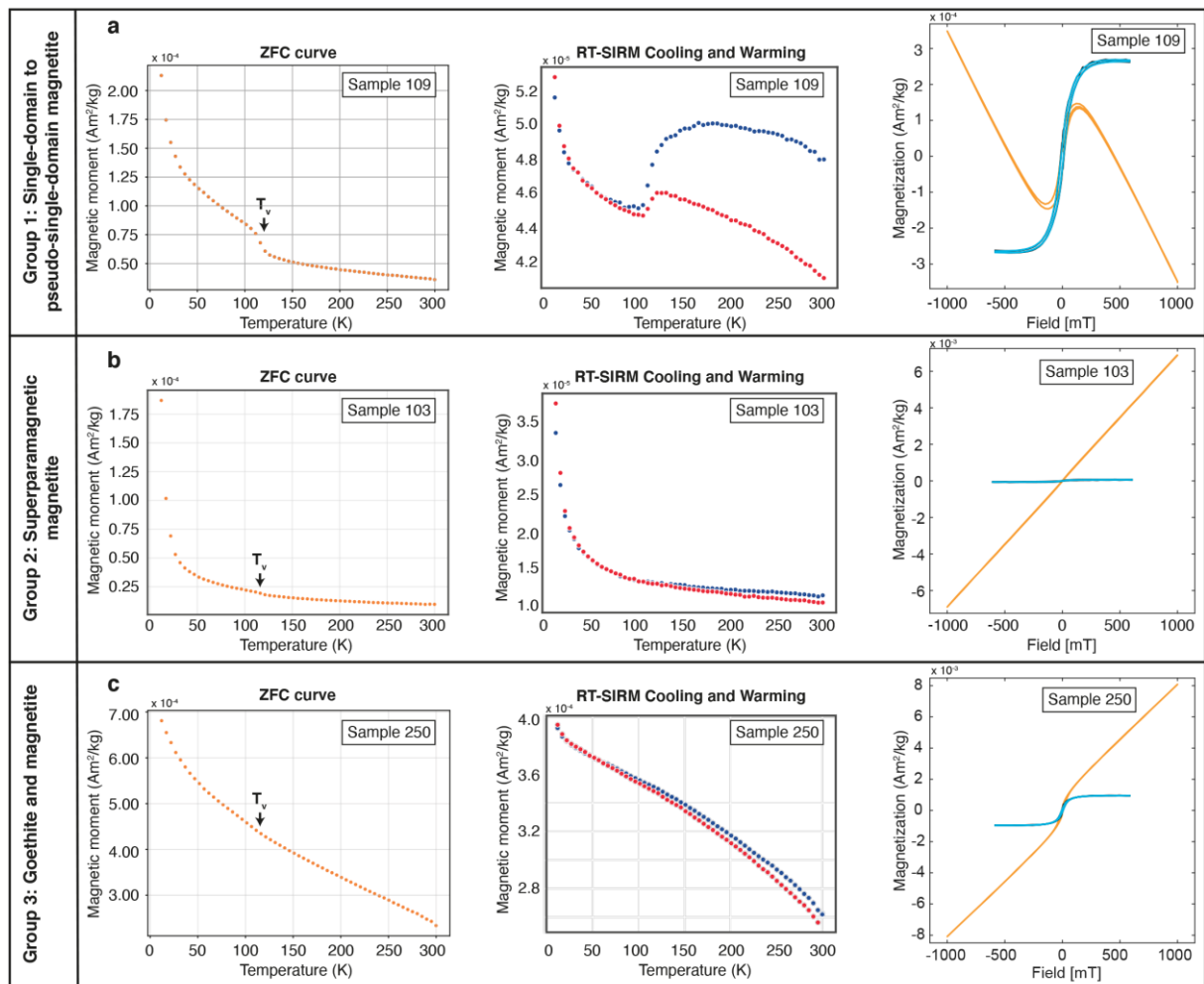


1042
 1043 Figure 1: (a) Simplified structural map of the western High Atlas in Morocco, modified
 1044 from El Bamiki et al. (2020). (b) Detailed lithostratigraphic column of the Erguita
 1045 section with interpreted regressive and transgressive trends. (c) Gamma-ray curve
 1046 showing the U content within the sediments. It is assumed that U reflects the
 1047 proportion of phosphate minerals because of their great incorporation of trace
 1048 elements, including U, compared to carbonates, sandstones, and marls (Aubineau et
 1049 al., 2022a; Nathan, 1984).

1050



1051
 1052 Figure 2: Facies and sedimentological features. (a) Gypsum layers (arrows) in the
 1053 basal Erguita section. (b) Massive P-rich carbonated sandstones. Note that these
 1054 rocks are sometimes crumbly. (c) Hummocky cross-stratification. (d) Finning-upward
 1055 gravity-flow deposit. (e) Nautiloid. (f) *Turritella* and *Oenopota* gastropods. (g) Massive
 1056 shell bed composed of oyster fragments. (h) Alternating carbonates and clayey
 1057 calcarenites in the uppermost part of the section. (i) Example of oriented cylindrical
 1058 cores consisting of P-rich calcarenite. Arrows show mm-sized, unsorted phosphatic
 1059 grains. Scale bar: 5 cm. Sample number is indicated in the white rectangle. Coin
 1060 diameters: 2.4 cm in (d, f) and 2.7 cm in (e). Hammer and pen lengths: 33 and 15
 1061 cm, respectively.



1062

1063

1064

1065

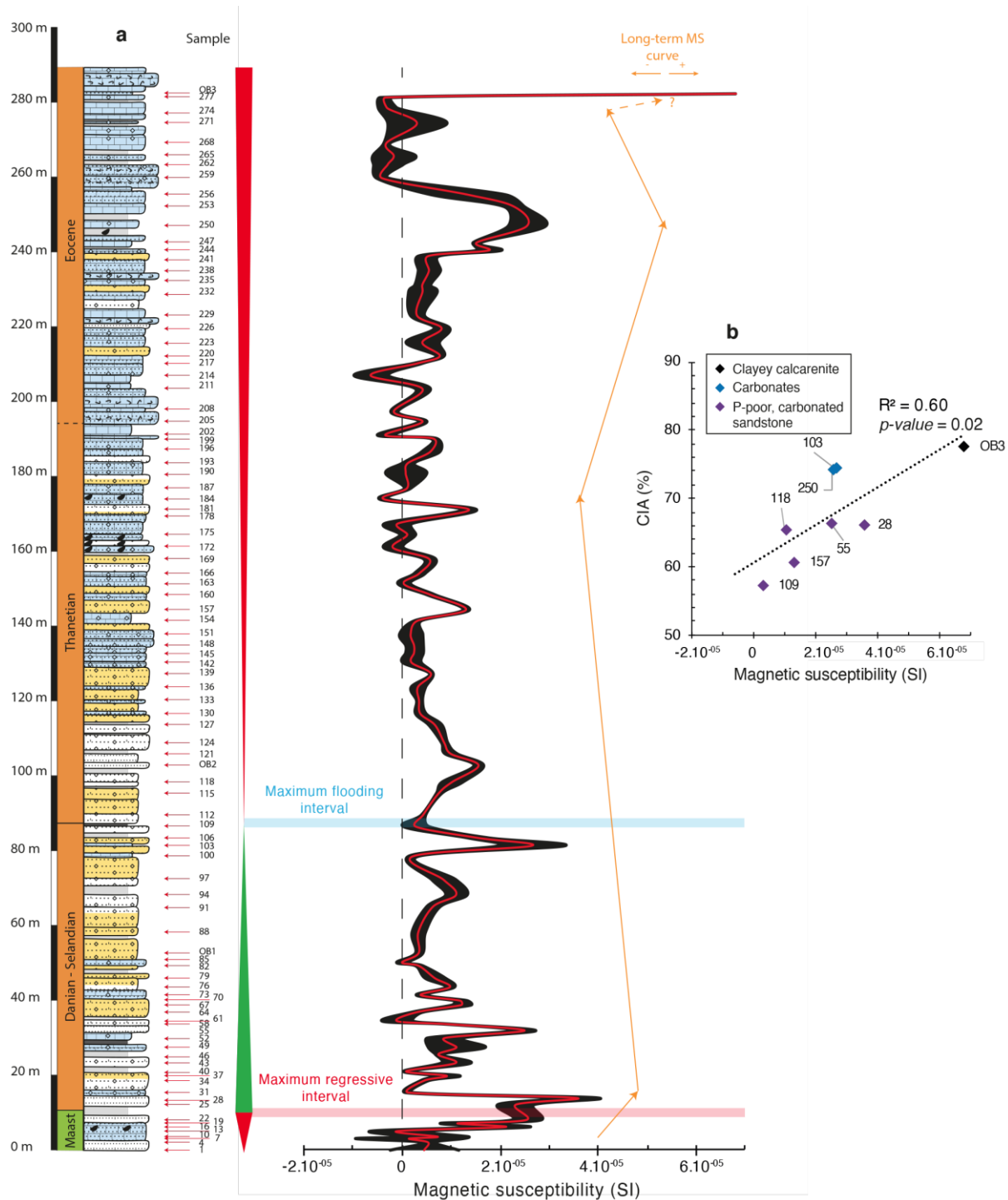
1066

1067

1068

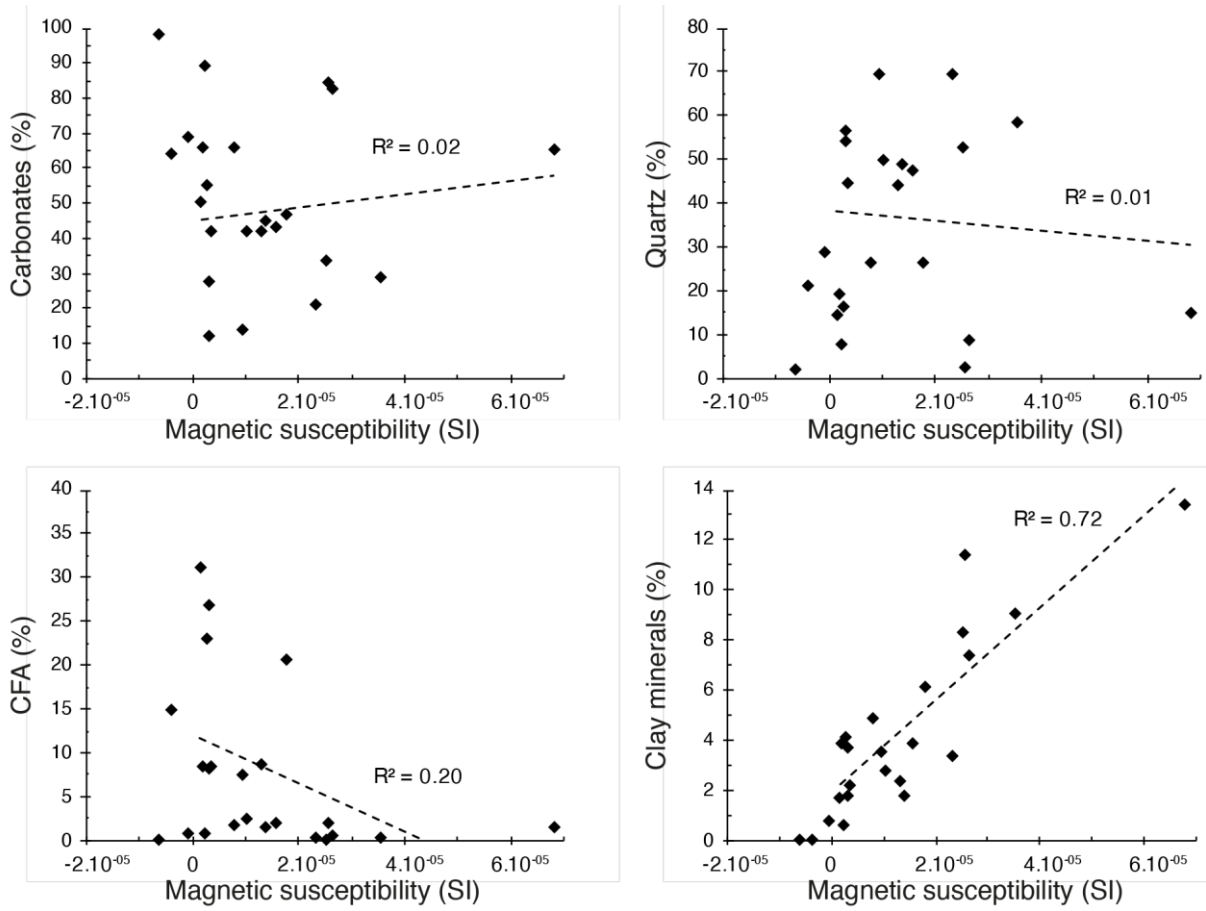
1069

Figure 3: Rock-magnetism data of the Erguita sediments. (a) Group 1 corresponding to single-domain to pseudo-single-domain magnetite. (b) Group 2 corresponding to superparamagnetic magnetite. (c) Group 3 corresponding to a mixture of iron oxides and iron oxyhydroxide minerals. Left panel, ZFC (zero field cooled) curve with the apparent Verwey transition (T_v); middle panel, mass-normalized RT-SIRM cycles, warming (in red) and cooling (in blue); right panel, uncorrected (orange) and corrected (blue) hysteresis loops.



1070
 1071 Figure 4: (a) Magnetic susceptibility curve (SI) with interpreted transgressive-
 1072 regressive trends in the Upper Cretaceous/Paleogene succession at Erguita. The red
 1073 line corresponds to the mean MS values, while the black line is the mean MS values
 1074 with one standard deviation. Legend of the lithostratigraphic column is on Figure 1.
 1075 The stratigraphy is based on El Bamiki et al. (2020). (b) Scatter plot between the
 1076 chemical index of alteration and magnetic susceptibility. P-rich sediments are not
 1077 shown because their formation falsifies the CIA values.

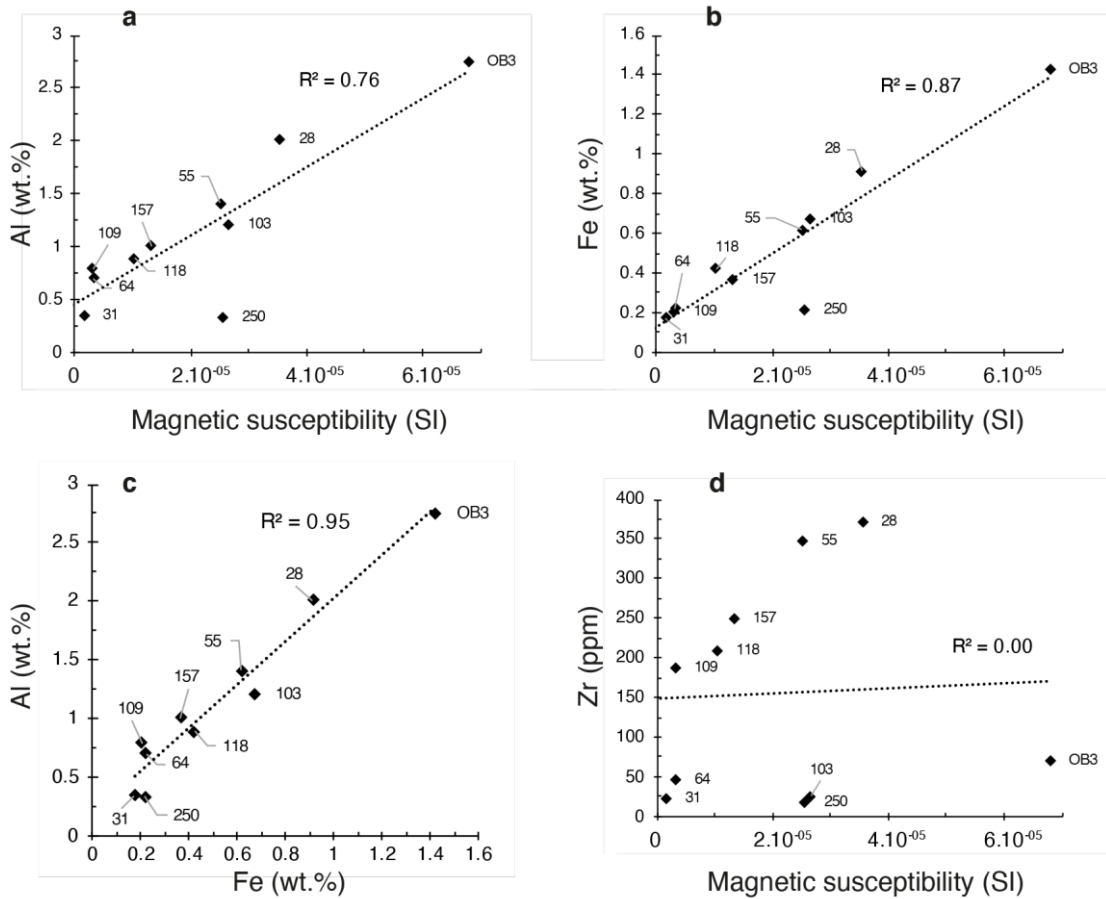
1078



1079

1080 Figure 5: Relationship between the proportion of most abundant mineral phases and
1081 magnetic susceptibility in the Erguita sediments. Linear regressions are shown
1082 without the incorporation of negative MS values.

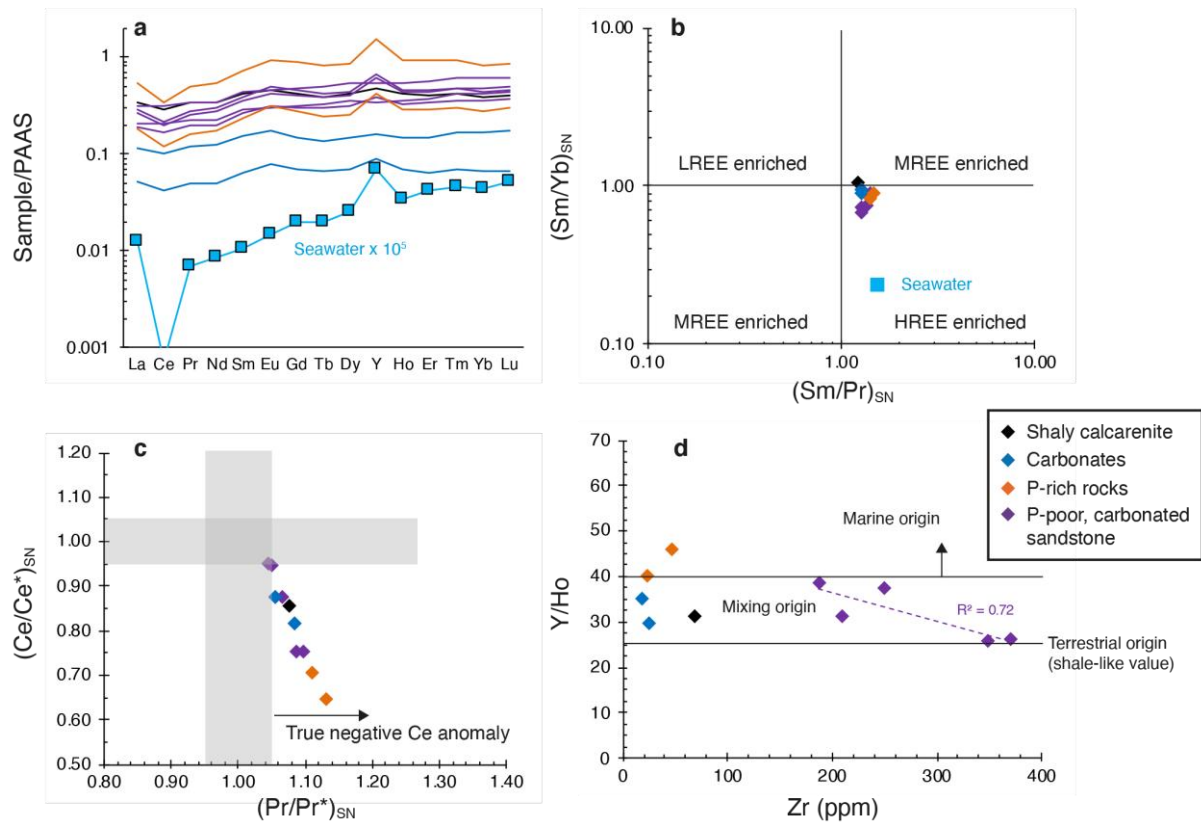
1083



1084

1085 Figure 6: Scatter plots showing the relationships between Al and MS (a), Fe and MS

1086 (b), Al and Fe (c), and Zr and MS (d).



1087

1088

1089

1090

1091

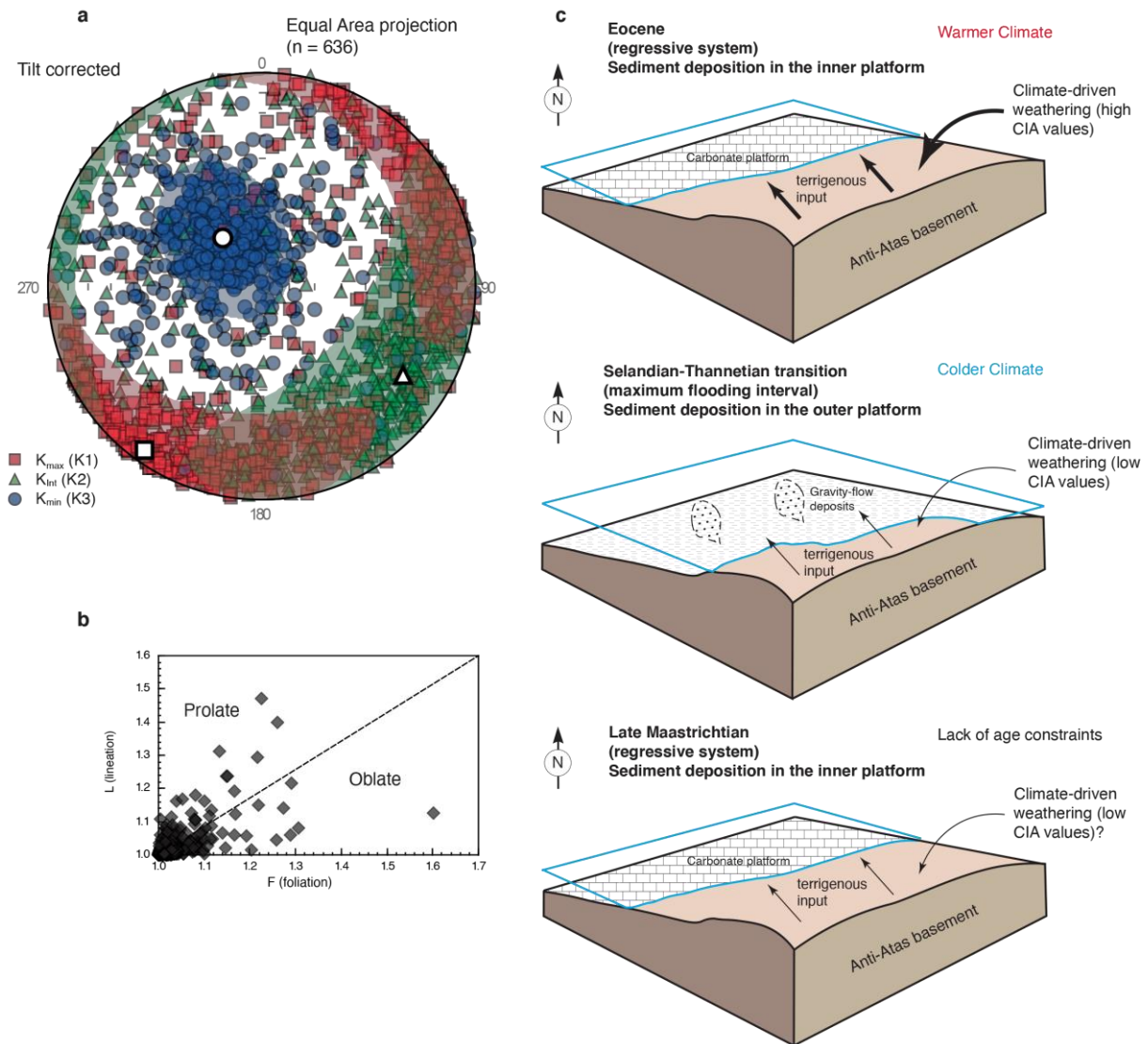
1092

1093

1094

1095

Figure 7: REEY geochemistry of the Erguita section. (a) Average PAAS-normalized REEY patterns compared to modern seawater (Alibo and Nozaki, 1999). Light (L)REE (La to Nd), Middle (M)REE (Sm to Dy), and Heavy (H)REE (Ho to Lu). Geochemical data of PAAS are from Taylor and McLennan (1985). (b) $(\text{Sm}/\text{Yb})_{\text{SN}}$ vs. $(\text{Sm}/\text{Pr})_{\text{SN}}$, after Garnit et al. (2012). Data of SW are from Alibo and Nozaki (1999). (c) Ce anomaly vs. Pr anomaly, after Bau and Dulski (1996). (d) Cross plot between Y/Ho and Zr showing the source of REE within the depositional environments. The Y/Ho ratios indicate a mixing source of REE.



1096

1097 Figure 8: (a) Data plotted on a lower hemisphere stereonet projection showing the
 1098 magnetic grain fabric. This projection derives from the AMS ellipsoid (for a
 1099 comprehensive illustration see Zhang et al. (2010) and Bilardello (2021). K_{min} is
 1100 vertical and K_{max} and K_{int} axes are randomly distributed within the horizontal plane,
 1101 which indicates deposition of particles under gravity only. (b) Flinn diagram (Flinn,
 1102 1978) of AMS data showing a minimum degree of anisotropy due to the presence of
 1103 both oblate (disk-shaped) and prolate (rod-shaped) particles. (c) 3D paleogeographic
 1104 model illustrating the weathering intensity that controls the magnetic mineral
 1105 proportions between the late Maastrichtian and Eocene. In this study, sea level
 1106 changes and MS vary independently. Both phyllosilicates and ferromagnetic minerals
 1107 likely contribute to the MS signal.

1108 **Tables and table legend**

1109 Table 1: Semi-quantification of the mineralogical assemblages in the Erguita
 1110 sediments. Data were obtained after careful examination of bulk XRD patterns.

Sample	Lithology	Height (m)	Calcite (%)	Dolomite† (%)	Dolomite‡ (%)	CFA (%)	Quartz (%)	K-Feldspars (%)	Smectite (%)	Illite/Mica (%)	Palygorskite (%)	Chlorite (%)	Kaolinite (%)	Clays total (%)	Gypsum and/or pyrite (%)
OB3	Clayey calcarenite	282.5		25	41	1	15			5	8	1		13	1
259	Sandy shell bed	259.9	60		4	15	21								
250	Carbonates	247.1	0.3	46	38	2	3		11					11	
244	P-rich calcarenite	240.6			47	21	26		6					6	
220	Calcarenite	212.4	10	16	40	2	26		5					5	1
214	Carbonates	207.2		0.2	98		2								
181	P-poor, carbonated sandstone	171.3		14	31	1	49	3		1	1			2	
178	Calcarenite	167.6		30	39	1	29	0.4		1				1	1
166	Calcarenite	154.2		20	22	8	45	3		2		1		2	
157	P-rich, carbonated sandstone	144.5	0.1	20	22	9	44	3		1		1		2	
151	Calcarenite	138	3	21	42	8	19	3		4				4	
145	P-rich calcarenite	133			55	23	17	1	4					4	
OB2	P-poor, carbonated sandstone	102.9			43	2	48	3		2			2	4	1
118	P-rich, carbonated sandstone	98.4		14	28	2	50	3		1			1	3	
109b	P-rich, carbonated sandstone	87.6	2	12	15	4	51	5	8				1	10	2
109a'	P-rich, carbonated sandstone	87	2	6	6	5	74	3	5					5	
109a	Muds	86.9		6	9	3	52		11	15			3	29	1
109	P-poor, carbonated sandstone	86.5	5	9	13	8	57	4		1			3	4	
106a	P-poor, carbonated sandstone	85.4	1	13	13	4	56	4	7				4	7	4
103	Carbonates	81.4		21	62	1	9		7					7	1
100	Carbonates	78.6		25	64	1	8	0.4		1				1	1
64	P-rich, carbonated sandstone	36.9	5		7	27	54	5	2					2	
58	P-poor, carbonated sandstone	33.7	9	2	3	8	69	4		1			2	4	2
55	P-poor, carbonated sandstone	32	1		33	0.1	53	4	7	2				8	2
31	P-rich calcarenite	15.4	1		49	31	14	2	2					2	1
28	P-poor, carbonated sandstone	13.3			29	0.2	58	3		7	2	0.2		9	
25	P-poor, carbonated sandstone	12.2			21	0.2	69	6		2	1	0.4		3	

1111
 1112 Note: Dolomite†, Ca-Mg (55:45); Dolomite‡, Ca-Mg (50:50); CFA, carbonate
 1113 fluorapatite

1114
 1115 Table 2: Major and trace element compositions and CIA values of representative
 1116 Erguita sediments.

Samples	OB3	250	157	118	109	103	64	55	31	28
Lithologies	Clayey calcarenite	Carbonates	P-rich, carbonated sandstone	P-rich, carbonated sandstone	P-poor, carbonated sandstone	Carbonates	P-rich, carbonated sandstone	P-poor, carbonated sandstone	P-rich calcarenite	P-poor, carbonated sandstone
Height (m)	282.5	247.1	144.5	98.4	86.5	81.4	36.9	32	15.4	13.3
SiO ₂ (%)	27.64	5.00	47.39	53.26	57.01	14.14	51.15	61.13	15.76	59.13
Al ₂ O ₃ (%)	5.20	0.62	1.91	1.69	1.49	2.28	1.32	2.66	0.64	3.80
Fe ₂ O ₃ (%)	2.04	0.31	0.52	0.60	0.29	0.97	0.32	0.88	0.25	1.30
MnO (%)	b.d.	b.d.	b.d.	0.019	0.018	0.020	b.d.	0.023	b.d.	0.032
MgO (%)	12.03	17.73	7.61	8.20	4.78	15.94	1.46	6.16	9.55	7.00
CaO (%)	19.28	30.60	17.12	13.55	15.70	24.54	21.95	10.09	33.01	9.61
Na ₂ O (%)	0.13	0.06	0.15	0.06	0.11	0.07	0.40	0.06	0.48	0.10
K ₂ O (%)	1.00	b.d.	0.68	0.66	0.71	0.52	0.79	1.07	0.33	1.51
TiO ₂ (%)	0.30	0.034	0.19	0.18	0.12	0.12	0.077	0.28	0.033	0.37
P ₂ O ₅ (%)	1.02	0.65	3.32	0.89	3.31	0.35	10.80	b.d.	11.06	0.17
LOI (%)	30.35	43.69	19.97	19.74	15.01	39.95	9.80	16.15	26.24	16.56
Total	99.0	98.7	98.9	98.8	98.5	98.9	98.1	98.5	97.4	99.6
CIA	77.5	74.1#	60.6	65.3	57.2	74.3	-	66.4	-	66.0
La (ppm)	13.15	2.00	10.23	7.13	10.76	4.41	20.85	7.90	6.83	11.97
Ce (ppm)	23.22	3.30	15.74	13.30	16.68	8.17	26.80	16.18	9.62	24.79
Pr (ppm)	2.98	0.43	2.28	1.72	2.43	1.05	4.38	1.96	1.43	3.02
Nd (ppm)	11.38	1.67	9.24	6.75	10.08	4.14	18.27	7.43	5.83	11.64
Sm (ppm)	2.27	0.35	1.94	1.44	2.17	0.83	4.03	1.58	1.27	2.41
Eu (ppm)	0.49	0.08	0.45	0.34	0.53	0.19	1.01	0.33	0.33	0.50
Gd (ppm)	1.97	0.33	1.87	1.38	2.13	0.69	4.16	1.45	1.29	2.23
Tb (ppm)	0.30	0.05	0.29	0.23	0.32	0.11	0.62	0.25	0.19	0.37
Dy (ppm)	1.92	0.32	1.91	1.48	2.05	0.69	3.96	1.62	1.21	2.48
Ho (ppm)	0.41	0.07	0.43	0.33	0.46	0.14	0.90	0.36	0.28	0.54
Er (ppm)	1.15	0.19	1.25	0.95	1.28	0.42	2.59	1.03	0.81	1.57
Tm (ppm)	0.17	0.03	0.19	0.15	0.19	0.07	0.37	0.17	0.12	0.25
Yb (ppm)	1.10	0.19	1.32	1.00	1.22	0.47	2.28	1.19	0.78	1.69
Lu (ppm)	0.17	0.03	0.21	0.16	0.20	0.08	0.37	0.19	0.13	0.27
Y (ppm)	12.79	2.40	16.10	10.21	17.72	4.32	41.38	9.20	11.26	14.19
Zr (ppm)	69.12	18.45	248.90	208.97	186.96	24.69	46.76	348.39	22.83	371.13
(La/Yb) _{SN}	0.88	0.79	0.58	0.53	0.66	0.70	0.68	0.49	0.65	0.53

1117
 1118 Note: LOI, loss on ignition; CIA, chemical index of alteration; b.d., below detection; -,
 1119 not calculated; #, we used K₂O = 0.03, which is the value of the detection limit; SN,
 1120 normalization to PAAS.